

# **SARS-CoV-2 spike S375F mutation characterizes the Omicron BA.1 variant**

Izumi Kimura<sup>1,18</sup>, Daichi Yamasoba<sup>1,2,18</sup>, Hesham Nasser<sup>3,4,18</sup>, Jiri Zahradnik<sup>5,18</sup>, Yusuke Kosugi<sup>1,6,18</sup>, Jiaqi Wu<sup>7,8,18</sup>, Kayoko Nagata<sup>9</sup>, Keiya Uriu<sup>1,6</sup>, Yuri L Tanaka<sup>10</sup>, Jumpei Ito<sup>1</sup>, Ryo Shimizu<sup>3</sup>, Toong Seng Tan<sup>11</sup>, Erika P Butlertanaka<sup>10</sup>, Hiroyuki Asakura<sup>12</sup>, Kenji Sadamasu<sup>12</sup>, Kazuhisa Yoshimura<sup>12</sup>, Takamasa Ueno<sup>11</sup>, Akifumi Takaori-Kondo<sup>9</sup>, Gideon Schreiber<sup>5</sup>, The Genotype to Phenotype Japan (G2P-Japan) Consortium, Mako Toyoda<sup>11</sup>, Kotaro Shirakawa<sup>9</sup>, Takashi Irie<sup>13</sup>, Akatsuki Saito<sup>10,14,15</sup>, So Nakagawa<sup>7,8\*</sup>, Terumasa Ikeda<sup>3\*</sup>, Kei Sato<sup>1,6,8,16,17,19,20\*</sup>.

<sup>1</sup> Division of Systems Virology, Department of Infectious Disease Control, The Institute of Medical Science, The University of Tokyo, Tokyo 1088639, Japan.

<sup>2</sup> Faculty of Medicine, Kobe University, Kobe 6500017, Japan.

<sup>3</sup> Division of Molecular Virology and Genetics, Joint Research Center for Human Retrovirus infection, Kumamoto University, Kumamoto 8600811, Japan.

<sup>4</sup> Department of Clinical Pathology, Faculty of Medicine, Suez Canal University, Ismailia 41511, Egypt.

<sup>5</sup> Department of Biomolecular Sciences, Weizmann Institute of Science, Rehovot 76100, Israel.

<sup>6</sup> Graduate School of Medicine, The University of Tokyo, Tokyo 1130033, Japan.

<sup>7</sup> Department of Molecular Life Science, Tokai University School of Medicine, Isehara 2591193, Japan.

<sup>8</sup> CREST, Japan Science and Technology Agency, Kawaguchi 3220012, Japan.

<sup>9</sup> Department of Hematology and Oncology, Graduate School of Medicine, Kyoto University, Kyoto 6068507, Japan.

<sup>10</sup> Department of Veterinary Science, Faculty of Agriculture, University of Miyazaki, Miyazaki 8892192, Japan.

<sup>11</sup> Division of Infection and immunity, Joint Research Center for Human Retrovirus infection, Kumamoto University, Kumamoto 8600811, Japan.

<sup>12</sup> Tokyo Metropolitan Institute of Public Health, Tokyo 1690073, Japan.

<sup>13</sup> Institute of Biomedical and Health Sciences, Hiroshima University, Hiroshima 7398511, Japan.

<sup>14</sup> Center for Animal Disease Control, University of Miyazaki, Miyazaki 8892192, Japan.

<sup>15</sup> Graduate School of Medicine and Veterinary Medicine, University of Miyazaki, Miyazaki 8892192, Japan.

<sup>16</sup> International Research Center for Infectious Diseases, The Institute of Medical Science, The University of Tokyo, Tokyo 1088639, Japan.

<sup>17</sup> International Vaccine Design Center, The Institute of Medical Science, The University of Tokyo, Tokyo 1088639, Japan.

42 <sup>18</sup> These authors contributed equally

43 <sup>19</sup> Twitter: @SystemsVirology

44 <sup>20</sup> Lead Contact

45

46 \*Corresponding authors:

47 so@tokai.ac.jp (So Nakagawa);

48 ikedat@kumamoto-u.ac.jp (Terumasa Ikeda);

49 KeiSato@g.ecc.u-tokyo.ac.jp (Kei Sato)

50

51 **Conflict of interest:** The authors declare that no competing interests exist.

52 **Short title:** Impact of S375F spike mutation (42/50 characters)

53 **Keywords:** SARS-CoV-2; COVID-19; Omicron; BA.2; BA.1; B.1.1.529;

54 pathogenicity; fusogenicity; transmissibility

## 55 **Abstract**

56 Recent studies have revealed the unique virological characteristics of Omicron,  
 57 the newest SARS-CoV-2 variant of concern, such as pronounced resistance to  
 58 vaccine-induced neutralizing antibodies, less efficient cleavage of the spike  
 59 protein, and poor fusogenicity. However, it remains unclear which mutation(s) in  
 60 the spike protein determine the virological characteristics of Omicron. Here, we  
 61 show that the representative characteristics of the Omicron spike are determined  
 62 by its receptor-binding domain. Interestingly, the molecular phylogenetic  
 63 analysis revealed that the acquisition of the spike S375F mutation was closely  
 64 associated with the explosive spread of Omicron in the human population. We  
 65 further elucidate that the F375 residue forms an interprotomer pi-pi interaction  
 66 with the H505 residue in another protomer in the spike trimer, which confers the  
 67 attenuated spike cleavage efficiency and fusogenicity of Omicron. Our data shed  
 68 light on the evolutionary events underlying Omicron emergence at the molecular  
 69 level.

70

71

## 72 **Highlights**

- 73 ● Omicron spike receptor binding domain determines virological
- 74 characteristics
- 75 ● Spike S375F mutation results in the poor spike cleavage and fusogenicity
- 76 in Omicron
- 77 ● Acquisition of the spike S375F mutation triggered the explosive spread of
- 78 Omicron
- 79 ● F375-H505-mediated  $\pi$ - $\pi$  interaction in the spike determines the
- 80 phenotype of Omicron

# 81 Introduction

82 Since the emergence of SARS-CoV-2 at the end of 2019, this virus has  
83 diversified spectacularly. In April 2022, the WHO defined two variants of concern,  
84 Delta (B.1.617.2 and AY lineages) and Omicron (originally the B.1.1.529 lineage,  
85 then reclassified into BA lineages) ([WHO, 2022](#)); and currently, Omicron is the  
86 predominant variant spreading worldwide.

87 Even before the emergence of the Omicron B.1.1.529 lineage at the  
88 end of November 2021 in South Africa ([National Institute for Communicable  
89 Diseases, 2021](#)), SARS-CoV-2 was highly diversified from the original lineage,  
90 the B lineage, which was isolated in Wuhan, China, on December 24, 2019  
91 (strain Wuhan-Hu-1, GISAID ID: EPI\_ISL\_402123) ([Wu et al., 2020](#)). Focusing  
92 on the evolutionary scenario leading to the emergence of Omicron, the B.1  
93 lineage, which has acquired the D614G mutation in the spike (S) protein ([Hou et  
94 al., 2020](#); [Korber et al., 2020](#); [Li et al., 2020](#); [Plante et al., 2020](#); [Yurkovetskiy et  
95 al., 2020](#)), was first reported on January 24, 2020 (GISAID ID: EPI\_ISL\_451345).  
96 Thereafter, the B.1.1 lineage was first reported in England on February 16, 2020  
97 (GISAID ID: EPI\_ISL\_466615). The B.1.1 lineage is the common ancestor of  
98 Alpha (B.1.1.7 lineage), a prior variant of concern by March 2022, and Omicron  
99 (B.1.1.529 lineage), and the Alpha variant caused a large surge of infection  
100 worldwide from the fall of 2020 ([Davies et al., 2021](#)). Omicron was first reported  
101 in South Africa on September 30, 2021 (GISAID ID: EPI\_ISL\_7971523)  
102 ([National Institute for Communicable Diseases, 2021](#)).

103 Soon after the press briefing on Omicron emergence on November 25,  
104 2021 ([National Institute for Communicable Diseases, 2021](#)), the virological  
105 characteristics of Omicron, currently designated BA.1 (i.e., B.1.1.529.1 lineage,  
106 hereafter, the BA.1 lineage is referred to as Omicron in this study), was  
107 intensively investigated. For example, Omicron exhibits profound resistance to  
108 the humoral immunity induced by vaccination and natural SARS-CoV-2 infection  
109 ([Cameroni et al., 2021](#); [Cao et al., 2021](#); [Carreño et al., 2021](#); [Cele et al., 2021](#);  
110 [Dejnirattisai et al., 2022](#); [Dejnirattisai et al., 2021](#); [Garcia-Beltran et al., 2021](#); [Liu  
111 et al., 2021](#); [Meng et al., 2022](#); [Planas et al., 2021](#); [Takashita et al., 2022](#);  
112 [VanBlargan et al., 2022](#)). Additionally, we demonstrated that Omicron S is less  
113 prone to cleavage by furin, a cellular protease, and exhibits poor fusogenicity  
114 ([Meng et al., 2022](#); [Suzuki et al., 2022](#)). However, it remains unclear why  
115 Omicron has spread so rapidly worldwide. In addition, although the explosive  
116 infectious spread of Omicron in the human population can be mainly  
117 characterized by the virological properties of Omicron S, the mutation(s) in  
118 Omicron S that are responsible for its virological characteristics, such as  
119 inefficient S cleavage, lower fusogenicity and profound immune resistance, have  
120 not been determined.

121           In this study, we first demonstrate that the representative  
 122 characteristics of Omicron S, such as immune resistance, poor S cleavage  
 123 efficiency and poor fusogenicity, are determined by its receptor-binding domain  
 124 (RBD). By molecular phylogenetic analysis, we show that the acquisition of the  
 125 S375F mutation in the Omicron RBD is closely associated with the explosive  
 126 spread of Omicron. Moreover, we experimentally demonstrate that the S375F  
 127 mutation is critical for the virological properties of Omicron S, namely, the  
 128 attenuation of S cleavage efficiency and fusogenicity. Furthermore, we elucidate  
 129 how the attenuated S cleavage and fusogenicity are conferred by the S375F  
 130 mutation.

## 131 Results

### 132 Omicron RBD determines the virological features of Omicron

133 To determine the mutation(s) responsible for the virological features of Omicron,  
 134 we prepared a series of expression plasmids for the Omicron S-based chimeric  
 135 mutants swapped with the N-terminal domain (NTD) and/or RBD of B.1  
 136 (D614G-bearing strain) S (**Figure 1A**). Pseudovirus experiments showed that  
 137 the pseudovirus with the B.1 RBD-bearing Omicron S [Omicron S/B.1 S\_RBD  
 138 (spike 4 in **Figure 1A**) and Omicron S/B.1 S\_NTD+RBD (spike 5)] exhibited  
 139 increased infectivity compared to that with Omicron S (spike 2) (**Figure 1B**).  
 140 Western blot analysis showed that the cleavage efficacy of Omicron S was lower  
 141 than that of B.1 S, which is consistent with our recent studies ([Meng et al., 2022](#);  
 142 [Suzuki et al., 2022](#); [Yamasoba et al., 2022](#)) (lanes 1 and 2 in **Figures 1C and**  
 143 **1D**). However, the chimeric Omicron S proteins bearing the B.1 RBD (spikes 4  
 144 and 5) showed increased cleavage efficacy (**Figures 1C and 1D**). Although the  
 145 surface expression levels of a series of S chimeras bearing the B.1 domains  
 146 (spikes 3-5) were lower than those of Omicron S chimeras (**Figure 1E**), a  
 147 cell-based fusion assay ([Motozono et al., 2021](#); [Saito et al., 2022](#); [Suzuki et al.,](#)  
 148 [2022](#); [Yamasoba et al., 2022](#)) revealed that the fusogenicity of the B.1  
 149 RBD-bearing Omicron S was significantly higher than that of the parental  
 150 Omicron S (**Figure 1F**). To verify the importance of the RBD for the phenotype of  
 151 Omicron S, we performed reversal experiments based on the B.1 S [B.1  
 152 S/Omicron S\_RBD (spike 6) in **Figure 1A**]. Corresponding to the results for  
 153 Omicron S, the pseudovirus infectivity (**Figure 1B**), S cleavage efficacy (**Figures**  
 154 **1C and 1D**), and fusogenicity (**Figures 1F**) of the Omicron RBD-harboring S  
 155 [B.1 S/Omicron S\_RBD (spike 6)] were attenuated compared to those of  
 156 parental B.1 S. These results suggest that the RBD of Omicron S determines the  
 157 virological characteristics of Omicron.

158 To further investigate the impact of the Omicron S RBD, we generated  
 159 a series of recombinant chimeric SARS-CoV-2 strains by reverse genetics  
 160 (**Figure 1G**) ([Torii et al., 2021](#)). As shown in **Figure 1H**, the growth of rOmicron  
 161 S-GFP (virus II) and rOmicron S/B.1 S\_NTD (virus III) was lower than that of  
 162 rB.1 S-GFP (virus I). However, the recombinant viruses bearing the B.1 RBD  
 163 [rOmicron S/B.1\_RBD-GFP (virus IV) and rOmicron S/B.1 S\_NTD+RBD-GFP  
 164 (virus V)] replicated more efficiently than rOmicron S-GFP (virus II) in  
 165 VeroE6/TMPRSS2 cells (**Figure 1H**). Additionally, we measured the GFP  
 166 intensity in infected cell cultures using routine procedures and showed that the  
 167 GFP intensity of the cells infected with the recombinant viruses bearing the B.1  
 168 RBD was significantly higher than that of the cells infected with rOmicron S-GFP  
 169 (virus II) (**Figures 1I and S1**). These data suggest that the RBD of Omicron S  
 170 attenuates viral growth capacity in cell cultures. To evaluate the fusogenicity of  
 171 the chimeric viruses, we measured the level of GFP-positive cells. As shown in

**Figure 1J**, the GFP-positive area of the cells infected with the recombinant viruses at 48 hours post infection (h.p.i.) was significantly larger for viruses bearing the B.1 RBD [rOmicron S/B.1\_RBD-GFP (virus IV) and rOmicron S/B.1 S\_NTD+RBD-GFP (virus V)] than for rOmicron-GFP (virus II). Consistent with the results using S-expressing cells (**Figure 1F**), these findings suggest that the Omicron RBD attenuates viral fusogenicity. Moreover, the plaques formed by infection with rOmicron S/B.1 S\_RBD-GFP (virus IV) and rOmicron S/B.1 S\_NTD+RBD-GFP (virus V) were significantly larger than those formed by rOmicron S-GFP virus (virus II), while the plaques formed by rOmicron S-GFP (virus II) and rOmicron S/B.1 S\_NTD-GFP (virus III) were comparable (**Figure 1K**). Altogether, these results suggest that the RBD of Omicron S determines the virological features of this viral lineage, such as the attenuation of pseudovirus infectivity, S1/S2 cleavage efficacy and fusogenicity, of Omicron.

# **Omicron RBD mainly determines the immune resistance of Omicron**

We next assessed the domains of Omicron S that are associated with the profound immune resistance of Omicron (Cameroni *et al.*, 2021; Cao *et al.*, 2021; Carreño *et al.*, 2021; Cele *et al.*, 2021; Dejnirattisai *et al.*, 2022; Dejnirattisai *et al.*, 2021; Garcia-Beltran *et al.*, 2021; Liu *et al.*, 2021; Meng *et al.*, 2022; Planas *et al.*, 2021; Takashita *et al.*, 2022; VanBlargan *et al.*, 2022). Because the swapping of Omicron S with B.1 S NTD (Omicron S/B.1 S\_NTD, spike 3) severely decreased pseudovirus infectivity (**Figure 1B**), we performed neutralization assays using pseudoviruses with Omicron RBD-bearing B.1 S [Omicron S/B.1 S\_RBD (spike 4) and Omicron S/B.1 S\_NTD+RBD (spike 5) as well as the S proteins of Omicron (spike 2), Delta and B.1 (spike 1) (the list of sera used is shown in **Table S1**). Consistent with recent studies (Cameroni *et al.*, 2021; Cao *et al.*, 2021; Carreño *et al.*, 2021; Cele *et al.*, 2021; Dejnirattisai *et al.*, 2022; Dejnirattisai *et al.*, 2021; Garcia-Beltran *et al.*, 2021; Liu *et al.*, 2021; Meng *et al.*, 2022; Planas *et al.*, 2021; Takashita *et al.*, 2022; VanBlargan *et al.*, 2022), Omicron S (spike 2) was highly resistant to the vaccine sera [BNT162b2 (**Figure 2A**) and mRNA-1273 (**Figure 2B**)] as well as convalescent sera from individuals infected with early pandemic virus (collected before May 2020) (**Figure 2C**) or with the Delta variant (**Figure 2D**). In the cases of pseudoviruses with Omicron S/B.1 S\_RBD (spike 4) and Omicron S/B.1 S\_NTD+RBD (spike 5), these pseudoviruses were significantly more sensitive to vaccine sera (**Figures 2A and 2B**) and convalescent sera obtained from early pandemic virus-infected patients than Omicron S (spike 2) (**Figure 2C**). These results suggest that the RBD of Omicron S is closely associated with its pronounced resistance to antiviral humoral immunity elicited by vaccination or previous SARS-CoV-2 infection. Moreover, we used convalescent sera from hamsters infected with B.1.1 (note that the S gene sequences of B.1 and B.1.1 are identical) and



Omicron for the assay. As shown in **Figure 2E**, Omicron S (spike 2) was completely resistant to the B.1.1 convalescent sera, while it was sensitive to the Omicron convalescent sera. Notably, the chimeric Omicron S bearing the B.1 RBD [Omicron S/B.1 S\_RBD (spike 4) and Omicron S/B.1 S\_NTD+RBD (spike 5)] exhibited the opposite results: these chimeric pseudoviruses were sensitive to the B.1.1 convalescent sera (**Figure 2E**) but completely resistant to the Omicron convalescent sera (**Figure 2F**). These results further suggest that the Omicron RBD determines its immune resistance and can be a remarkable antigen for humoral immunity. However, we found that Omicron S/B.1 S\_NTD+RBD (spike 5) is significantly more sensitive to antisera than Omicron S/B.1 S\_RBD (spike 4) (**Figures 2A-2C and 2E**). These findings suggest that mutations in the NTD of Omicron S are also partly associated with the immune resistance of Omicron S.

### **S S375F mutation increases binding affinity to human ACE2**

In the RBD (residues 319-541), 12 substitutions were uniquely found in Omicron S, while the other 3 substitutions (K417N, T478K and N501Y) were commonly detected in the other variants (**Figure 3A**) (Meng *et al.*, 2022). To determine the residue(s) responsible for the virological phenotype of Omicron, we prepared a series of B.1 S RBD point mutants that bear the respective mutations of Omicron and conducted screening experiments based on a yeast surface display assay (Dejnirattisai *et al.*, 2022; Kimura *et al.*, 2022; Motozono *et al.*, 2021; Yamasoba *et al.*, 2022; Zahradnik *et al.*, 2021). As shown in **Figure 3B** (left panel), compared to the RBD of parental (i.e., B lineage-based) S, the  $K_D$  values of the G339D, N440K and S477N mutants significantly decreased, while those of the S375F, S371L/S373P/S375F, G496S and Y505H mutants significantly increased. Since the ACE2 binding affinity of Omicron S is lower than that of the RBD of ancestral (including B.1 lineage) SARS-CoV-2 (Dejnirattisai *et al.*, 2022; Yamasoba *et al.*, 2022), these data suggest that the S375F, G496S and Y505H substitutions are closely associated with the phenotypes of Omicron.

### **Evolution of Omicron is closely associated with the acquisition of the S S375F mutation**

The S375F, G496S and Y505H mutations in the S protein were almost exclusively detected in the Omicron variants (**Table S2**). To infer the evolutionary sequence of the emergence of these mutations in the lineage of Omicron, we generated a time tree of 48 Omicron genomes detected in 2021 (for more detail, see STAR METHODS) (**Figures 3C and S2**). The G496S and Y505H mutations were detected in all sequences used in this analysis, suggesting that these two mutations were acquired in the common ancestor of all Omicron variants reported so far. In contrast, the S371L, S373P and S375F



254 mutations were not included in the older Omicron sequences (shown in black in  
255 **Figures 3C and S2**). Although the emergence times of S371L and S373P  
256 cannot be estimated independently, our analysis assumed that the S371L and  
257 S373P mutations were first acquired between Node 1 [95% highest posterior  
258 density (HPD): September 2, 2021 to October 13, 2021] and Node 2 (95% HPD:  
259 September 28, 2021 to October 21, 2021) in **Figure 3C**, based on the estimated  
260 time to the most recent common ancestor (tMRCA). The S375F mutation  
261 emerged thereafter, between Node 2 and Node 3 (95% HPD: October 7, 2021 to  
262 October 23, 2021) (**Figure 3C**). Interestingly, the Bayesian skyline plot of the 48  
263 Omicron genomes suggested that the effective population size of Omicron  
264 increased just after the acquisition of the S375F substitution (**Figure 3D**). These  
265 data suggest that the emergence of the S375F mutation was a crucial event to  
266 trigger the massive spread of the Omicron variants in the human population.

267 To verify the possibility that the S375F mutation is crucial for the  
268 phenotype of Omicron, we performed yeast binding assays using the RBD of  
269 Omicron S. As shown in **Figure 3B** (right panel), the F375S and  
270 L371S/P373S/F375S mutations in the RBD of Omicron S significantly increased  
271 the binding affinity to human ACE2. Overall, these observations suggest that the  
272 three substitutions at positions 371, 373 and 375, and particularly the S375F  
273 substitution, determine the virological phenotype of Omicron.

274

## 275 **S S375F mutation determines the virological features of Omicron**

276 To investigate the impact of the S375F mutation, we prepared pseudoviruses  
277 with a series of Omicron S-based mutants (**Figure 4A**). Corresponding to the  
278 yeast surface display assay (**Figure 3B**), the gain-of-function assay showed that  
279 pseudovirus infectivity was clearly increased by the insertion of the F375S  
280 mutation (spikes 9 and 11-13 in **Figure 4A**) in Omicron S (**Figure 4B, top**).  
281 Western blot analysis showed that the S1/S2 cleavage efficacy was also  
282 rescued by the F375S mutation (**Figures 4C and 4D, top**). Although the surface  
283 S expression level was decreased by this mutation (**Figure 4E, top**), a  
284 cell-based fusion assay demonstrated that the F375S mutation significantly  
285 increased the efficacy of SARS-CoV-2 S-mediated cell-cell fusion (**Figure 4F,**  
286 **top**). Conversely, a loss-of-function assay based on the B.1 S showed that the  
287 S375F mutation (spikes 16 and 18-20) decreased pseudovirus infectivity  
288 (**Figure 4B, bottom**), S cleavage efficacy (**Figures 4C and 4D, bottom**) and  
289 fusion activity (**Figure 4F, bottom**). These results suggest that the S375F  
290 mutation in Omicron S is responsible for its virological phenotypes. However, the  
291 S371L/S373P/S375F mutations did not affect the sensitivity to the antiviral  
292 humoral immunity elicited by vaccination and infection (**Figure S3**), suggesting  
293 that these mutations are not associated with the immune resistant phenotype of  
294 Omicron.

To further assess the impact of the S375F mutation, we generated two additional recombinant chimeric SARS-CoV-2 strains, B.1 S S375F-GFP (virus VI) and Omicron S F375S-GFP (virus VII) (**Figure 5A**). Although the mutation at position 375 did not affect the viral RNA load in the culture supernatant of infected VeroE6/TMPRSS2 cells (**Figure 5B**), the GFP intensity in infected VeroE6/TMPRSS2 cells was modulated by the mutation at the position 375 of the S protein: the S375F mutation in the B.1 S backbone decreased the GFP intensity, while the F375S mutation in the Omicron S backbone increased the intensity (**Figures 5C and S1**). Additionally, quantitative fluorescence microscopy showed that the GFP-positive area of B.1 S S375F-GFP (virus VI) was significantly lower than that of parental B.1 S-GFP (virus I), while that of Omicron S F375S-GFP (virus VII) was significantly higher than that of parental Omicron S-GFP (virus II) (**Figure 5D**). Moreover, plaque assays showed that the plaques formed by infection with B.1 S S375F-GFP (virus VI) were significantly smaller than those formed by B.1 S-GFP (virus I), while conversely, the plaque size was increased by the insertion of the F375S mutation in Omicron S (**Figure 5E**). Altogether, these results suggest that the S375F mutation in the Omicron S protein determines the virological characteristics (decreased infectivity, decreased S1/S2 cleavage efficacy, and decreased fusogenicity) of Omicron.

### **The F375-H505 pi-pi interaction contributes to the virological phenotype of Omicron**

Here, we experimentally demonstrated that the S375F mutation determines the virological properties of Omicron (**Figures 4 and 5**). Additionally, molecular phylogenetic analysis suggested that the emergence of this mutation was closely associated with the explosive growth of Omicron in the human population (**Figures 3C and 3D**). However, it remains unclear how the S375F mutation contributes to the phenotype of Omicron at the molecular level. We addressed this question using a structural biology approach. As shown in **Figure 6A** (top), we predicted that the F375 residue in a fully closed Omicron S trimer can form a pi-pi interaction, a sort of dispersion by van der Waals forces between aromatic residues [reviewed in (Martinez and Iverson, 2012)], with the H505 residue in another S protein in the same trimer. Because residue 375 in the B.1.1 S protein is a serine, the pi-pi interaction cannot be formed (**Figure 6A, bottom**). To address the hypothesis that the F375-H505-mediated inter-protomer pi-pi interaction contributes to the phenotype of Omicron, we prepared the Omicron S H505A mutant in which an aromatic side chain at position 505 is disrupted. Western blot analysis showed that the S cleavage efficacy of Omicron S was increased by the insertion of the H505A mutation (**Figure 6B**). To further test this possibility, the residues at position 375 of B.1 S were substituted with amino acids bearing aromatic side chains (i.e., F, Y and H). Similar to the S375F

mutant, the B.1 S mutants bearing the S375Y or S375H mutation showed decreased cleavage efficacy of the S protein (**Figure 6C**). These results further suggest that the inter-protomer pi-pi interaction is formed between Y505 and S375F/Y/H. Moreover, the insertion of the Y505A mutation in the B.1 S bearing the S375F/Y/H mutation (i.e., the disruption of the aromatic residue at position 505) rescued the S cleavage efficacy (**Figure 6C**).

Finally, we verified the impact of the inter-protein pi-pi interaction on S-mediated fusogenicity. Although the Omicron S F375S mutant exhibited a decreased surface expression level, the H505A mutation did not (**Figure 6D**). In the case of the B.1 S-based mutants, the Y505A mutation decreased the surface expression levels when inserted together with the S375F/Y mutations (**Figure 6E**). Corresponding to the western blot results (**Figure 6B**), the disruption of the pi-pi interaction by F375S and H505A in Omicron S significantly increased fusion activity (**Figure 6F**). Moreover, in the case of the B.1 S-based mutant, the substitution of residue 375 with an aromatic residue (F, Y or H) significantly decreased the fusion activity (**Figure 6G**). However, when we inserted the Y505A substitution in the S375F/Y/H mutants to disrupt the aromatic residue at position 505, fusion activity was significantly increased (**Figure 6G**). Altogether, our results suggest that the inter-protomer pi-pi interaction mediated by the aromatic residues at positions 375 and 505 of the S protein contributes to decreased S cleavage efficacy and fusogenicity.

## 357 Discussion

358 In the present study, we performed multiscale investigations to unveil the  
359 virological characteristics of the Omicron variant of SARS-CoV-2. By using  
360 pseudoviruses, a yeast surface display system and the chimeric recombinant  
361 SARS-CoV-2 generated by reverse genetics, we showed that the RBD of  
362 Omicron S is responsible for the representative virological features of this variant.  
363 In particular, the S375F mutation in the RBD of Omicron S determines the  
364 characteristic virological properties of Omicron: decreased affinity to ACE2,  
365 decreased infectivity, decreased growth efficacy, attenuated efficacy of S  
366 cleavage, and reduced fusogenicity. Molecular phylogenetic analysis provided  
367 evidence suggesting that the acquisition of the S375F mutation was closely  
368 related to the onset of the explosive spread of Omicron in the human population.  
369 Furthermore, experiments based on structural biology revealed that the pi-pi  
370 interaction mediated by residues of F375 and H505 is responsible for the  
371 characteristics of Omicron S.

372 We provided evidence suggesting that the S375F mutation determines  
373 the virological features of Omicron. We also revealed that the nascent pi-pi  
374 interaction in the S trimer is established by the F375 and H505 residues and  
375 characterizes the Omicron S. Because the Y505H mutation was already  
376 acquired in the ancestral Omicron sequences, our results suggest that the  
377 acquisition of the S375F mutation during the evolution of Omicron rendered the  
378 properties of SARS-CoV-2 S protein to attenuate the S cleavage efficacy and  
379 fusogenicity, which led to the explosive spread of Omicron in the human  
380 population. The S375F mutation is highly conserved in the Omicron lineage and  
381 has not been detected in the other SARS-CoV-2 variants that have emerged to  
382 date. However, our data suggest that the substitution of residues possessing an  
383 aromatic ring, such as phenylalanine, tyrosine and histidine, at residue 375 can  
384 confer Omicron-like properties. Therefore, the emergence of SARS-CoV-2  
385 variants bearing such substitutions at residue 375 should be considered a  
386 potential risk for global health.

387

## 388 Limitations of the study

389 Here, we showed the importance of the S375F mutation to the virological  
390 properties of Omicron; however, the following issues remain unclear. First,  
391 although we showed that the S375F mutation determines the virological features  
392 of Omicron S, it remains unclear which mutations in Omicron S determine the  
393 pronounced immune resistance of Omicron S. Second, in addition to the  
394 Omicron BA.1 variant that we focused on this study, another recently emerged  
395 Omicron lineage, BA.2, also bears the S375F mutation. However, we have  
396 recently shown that the fusogenicity of BA.2 S is significantly higher than that of  
397 BA.1 S ([Yamasoba et al., 2022](#)). Together with the results shown in this study,

398 these observations suggest that BA.2 S acquired certain compensatory  
399 mutation(s) that increased fusion efficacy. Further investigations will be needed  
400 to unveil the full evolutionary history of the Omicron lineage. Furthermore, the  
401 question of why the acquisition of the S375F mutation caused explosive spread  
402 despite reducing infectivity in tissue culture, S cleavage efficacy and fusogenicity  
403 also needs to be elucidated in detail by further studies.

## 404 **Author Contributions**

405 Izumi Kimura, Daichi Yamasoba, Hesham Nasser, Yusuke Kosugi, Kayoko  
406 Nagata, Keiya Uriu, Yuri L Tanaka, Ryo Shimizu, Toong Seng Tan, Erika P  
407 Butlertanaka, Mako Toyoda, Takashi Irie, Akatsuki Saito and Terumasa Ikeda  
408 performed cell culture experiments.

409 Jiri Zahradnik and Gideon Schreiber performed a yeast surface display assay.

410 Jumpei Ito, Hiroyuki Asakura, Kenji Sadamasu and Kazuhisa Yoshimura  
411 performed viral genome sequencing analysis.

412 Takamasa Ueno, Akifumi Takaori-Kondo and Kotaro Shirakawa contributed  
413 clinical sample collection.

414 Jumpei Ito performed statistical analyses.

415 Jiri Zahradnik and Yusuke Kosugi performed structural analyses.

416 Jiaqi Wu and So Nakagawa performed molecular phylogenetic analyses.

417 Mako Toyoda, Kotaro Shirakawa, Takashi Irie, Akatsuki Saito, So Nakagawa,  
418 Terumasa Ikeda and Kei Sato designed the experiments and interpreted the  
419 results.

420 Kei Sato wrote the original manuscript.

421 All authors reviewed and proofread the manuscript.

422 The Genotype to Phenotype Japan (G2P-Japan) Consortium contributed to the  
423 project administration.

424

## 425 **Conflict of interest**

426 The authors declare that no competing interests exist.

427

## 428 **Acknowledgments**

429 We would like to thank all members belonging to The Genotype to Phenotype  
430 Japan (G2P-Japan) Consortium. We thank Dr. Kenzo Tokunaga (National  
431 Institute for Infectious Diseases, Japan) and Dr. Jin Gohda (The University of  
432 Tokyo, Japan) for providing reagents. The super-computing resource was  
433 provided by Human Genome Center at The University of Tokyo.

434 This study was supported in part by AMED Research Program on  
435 Emerging and Re-emerging Infectious Diseases (20fk0108268, to Akifumi  
436 Takaori-Kondo; 20fk0108517, to Akifumi Takaori-Kondo; 20fk0108146, to Kei  
437 Sato; 20fk0108270, to Kei Sato; 20fk0108413, to So Nakagawa, Terumasa  
438 Ikeda and Kei Sato; 20fk0108451, to Takamasa Ueno, Akifumi Takaori-Kondo,  
439 G2P-Japan Consortium, Takashi Irie, Akatsuki Saito, So Nakagawa, Terumasa  
440 Ikeda and Kei Sato); AMED Research Program on HIV/AIDS (21fk0410034, to  
441 Akifumi Takaori-Kondo; 21fk0410033, to Akatsuki Saito; and 21fk0410039, to  
442 Kei Sato); AMED CRDF Global Grant (21jk0210039 to Akatsuki Saito); AMED  
443 Japan Program for Infectious Diseases Research and Infrastructure  
444 (21wm0325009, to Akatsuki Saito); JST A-STEP (JPMJTM20SL, to Terumasa



Ikeda); JST SICORP (e-ASIA) (JPMJSC20U1, to Kei Sato); JST SICORP (JPMJSC21U5, to Kei Sato), JST CREST (JPMJCR20H6, to So Nakagawa; JPMJCR20H4, to Kei Sato); JSPS KAKENHI Grant-in-Aid for Scientific Research C (19K06382, to Akatsuki Saito); JSPS KAKENHI Grant-in-Aid for Scientific Research B (18H02662, to Kei Sato; and 21H02737, to Kei Sato); JSPS Fund for the Promotion of Joint International Research (Fostering Joint International Research) (18KK0447, to Kei Sato); JSPS Core-to-Core Program (A. Advanced Research Networks) (JPJSCCA20190008, to Kei Sato); JSPS Research Fellow DC1 (19J20488, to Izumi Kimura; xxxx, to Keiya Uriu); JSPS Leading Initiative for Excellent Young Researchers (LEADER) (to Terumasa Ikeda); The Tokyo Biochemical Research Foundation (to Kei Sato); Mitsubishi Foundation (to Terumasa Ikeda); Shin-Nihon Foundation of Advanced Medical Research (to Mako Toyoda and Terumasa Ikeda); Tsuchiya Foundation (to Takashi Irie); a Grant for Joint Research Projects of the Research Institute for Microbial Diseases, Osaka University (to Akatsuki Saito); an intramural grant from Kumamoto University COVID-19 Research Projects (AMABIE) (to Terumasa Ikeda); Intercontinental Research and Educational Platform Aiming for Eradication of HIV/AIDS (to Terumasa Ikeda); and Joint Usage/Research Center program of Institute for Frontier Life and Medical Sciences, Kyoto University (to Kei Sato).

465

## 466 **Consortia**

### 467 **The Genotype to Phenotype Japan (G2P-Japan) Consortium**

468 Shigeru Fujita<sup>1</sup>, Mai Suganami<sup>1</sup>, Akiko Oide<sup>1</sup>, Mika Chiba<sup>1</sup>, Naoko Misawa<sup>1</sup>,  
469 Takasuke Fukuhara<sup>21</sup>, Keita Matsuno<sup>21</sup>, Hirofumi Sawa<sup>21</sup>, Shinya Tanaka<sup>21</sup>,  
470 Tomokazu Tamura<sup>21</sup>, Rigel Suzuki<sup>21</sup>, Yuhei Morioka<sup>21</sup>, Kana Tsushima<sup>21</sup>,  
471 Haruko Kubo<sup>21</sup>, Naganori Nao<sup>21</sup>, Asako Shigeno<sup>21</sup>, Masumi Tsuda<sup>21</sup>, Mai  
472 Kishimoto<sup>21</sup>, Lei Wang<sup>21</sup>, Yoshitaka Oda<sup>21</sup>, Zannatul Ferdous<sup>21</sup>, Hiromi Mouri<sup>21</sup>,  
473 Miki Iida<sup>21</sup>, Keiko Kasahara<sup>21</sup>, Koshiro Tabata<sup>21</sup>, Mariko Ishizuka<sup>21</sup>, Kenzo  
474 Tokunaga<sup>22</sup>, Seiya Ozono<sup>22</sup>, Isao Yoshida<sup>12</sup>, Mami Nagashima<sup>12</sup>, Miyoko  
475 Takahashi<sup>7</sup>, Yasuhiro Kazuma<sup>9</sup>, Ryosuke Nomura<sup>9</sup>, Yoshihito Horisawa<sup>9</sup>,  
476 Yusuke Tashiro<sup>9</sup>, Yugo Kawai<sup>9</sup>, Ryoko Kawabata<sup>13</sup>, Otowa Takahashi<sup>3</sup>, Kimiko  
477 Ichihara<sup>3</sup>, Kazuko Kitazato<sup>3</sup>, Haruyo Hasebe<sup>3</sup>, Chihiro Motozono<sup>11</sup>, Isaac  
478 Ngare<sup>11</sup>

479

480 <sup>21</sup> Hokkaido University, Sapporo, Japan.

481 <sup>22</sup> National Institute of Infectious Diseases, Tokyo, Japan



# References

- 482 Cameroni, E., Bowen, J.E., Rosen, L.E., Saliba, C., Zepeda, S.K., Culap, K.,  
483 Pinto, D., VanBlargan, L.A., De Marco, A., di Iulio, J., et al. (2021). Broadly  
484 neutralizing antibodies overcome SARS-CoV-2 Omicron antigenic shift. *Nature*.  
485 10.1038/s41586-021-04386-2.  
486 Cao, Y., Wang, J., Jian, F., Xiao, T., Song, W., Yisimayi, A., Huang, W., Li, Q.,  
487 Wang, P., An, R., et al. (2021). Omicron escapes the majority of existing  
488 SARS-CoV-2 neutralizing antibodies. *Nature*, doi:  
489 <https://doi.org/10.1038/d41586-41021-03796-41586>.  
490 Carreño, J.M., Alshammary, H., Tcheou, J., Singh, G., Raskin, A., Kawabata, H.,  
491 Sominsky, L., Clark, J., Adelsberg, D.C., Bielak, D., et al. (2021). Activity of  
492 convalescent and vaccine serum against SARS-CoV-2 Omicron. *Nature*, doi:  
493 <https://doi.org/10.1038/d41586-41021-03846-z>.  
494 Cele, S., Jackson, L., Khoury, D.S., Khan, K., Moyo-Gwete, T., Tegally, H., San,  
495 J.E., Cromer, D., Scheepers, C., Amoako, D., et al. (2021). Omicron extensively  
496 but incompletely escapes Pfizer BNT162b2 neutralization. *Nature*, doi:  
497 <https://doi.org/10.1038/d41586-41021-03824-41585>.  
498 Chen, S., Zhou, Y., Chen, Y., and Gu, J. (2018). fastp: an ultra-fast all-in-one  
499 FASTQ preprocessor. *Bioinformatics* 34, i884-i890.  
500 10.1093/bioinformatics/bty560.  
501 Cingolani, P., Platts, A., Wang le, L., Coon, M., Nguyen, T., Wang, L., Land, S.J.,  
502 Lu, X., and Ruden, D.M. (2012). A program for annotating and predicting the  
503 effects of single nucleotide polymorphisms, SnpEff: SNPs in the genome of  
504 *Drosophila melanogaster* strain w1118; iso-2; iso-3. *Fly (Austin)* 6, 80-92.  
505 10.4161/fly.19695.  
506 Davies, N.G., Abbott, S., Barnard, R.C., Jarvis, C.I., Kucharski, A.J., Munday,  
507 J.D., Pearson, C.A.B., Russell, T.W., Tully, D.C., Washburne, A.D., et al. (2021).  
508 Estimated transmissibility and impact of SARS-CoV-2 lineage B.1.1.7 in England.  
509 *Science* 372. 10.1126/science.abg3055.  
510 Dejnirattisai, W., Huo, J., Zhou, D., Zahradnik, J., Supasa, P., Liu, C.,  
511 Duyvesteyn, H.M.E., Ginn, H.M., Mentzer, A.J., Tuekprakhon, A., et al. (2022).  
512 SARS-CoV-2 Omicron-B.1.1.529 leads to widespread escape from neutralizing  
513 antibody responses. *Cell* 185, 467-484 e415. 10.1016/j.cell.2021.12.046.  
514 Dejnirattisai, W., Shaw, R.H., Supasa, P., Liu, C., Stuart, A.S., Pollard, A.J., Liu,  
515 X., Lambe, T., Crook, D., Stuart, D.I., et al. (2021). Reduced neutralisation of  
516 SARS-CoV-2 omicron B.1.1.529 variant by post-immunisation serum. *Lancet*,  
517 doi:[https://doi.org/10.1016/S0140-6736\(1021\)02844-02840](https://doi.org/10.1016/S0140-6736(1021)02844-02840).  
518 Ferreira, I., Kemp, S.A., Datir, R., Saito, A., Meng, B., Rakshit, P.,  
519 Takaori-Kondo, A., Kosugi, Y., Uriu, K., Kimura, I., et al. (2021). SARS-CoV-2  
520 B.1.617 mutations L452R and E484Q are not synergistic for antibody evasion. *J*  
521 *Infect Dis* 224, 989-994. 10.1093/infdis/jiab368.  
522

523 Garcia-Beltran, W.F., Denis, K.J.S., Hoelzemer, A., Lam, E.C., Nitido, A.D.,  
524 Sheehan, M.L., Berrios, C., Ofoman, O., Chang, C.C., Hauser, B.M., et al.  
525 (2021). mRNA-based COVID-19 vaccine boosters induce neutralizing immunity  
526 against SARS-CoV-2 Omicron variant. *Cell*, doi:  
527 <https://doi.org/10.1016/j.cell.2021.1012.1033>.  
528 Hou, Y.J., Chiba, S., Halfmann, P., Ehre, C., Kuroda, M., Dinno, K.H., 3rd, Leist,  
529 S.R., Schafer, A., Nakajima, N., Takahashi, K., et al. (2020). SARS-CoV-2  
530 D614G variant exhibits efficient replication ex vivo and transmission in vivo.  
531 *Science* 370, 1464-1468. 10.1126/science.abe8499.  
532 Katoh, K., and Standley, D.M. (2013). MAFFT multiple sequence alignment  
533 software version 7: improvements in performance and usability. *Mol Biol Evol* 30,  
534 772-780. 10.1093/molbev/mst010.  
535 Kimura, I., Kosugi, Y., Wu, J., Zahradnik, J., Yamasoba, D., Butlertanaka, E.P.,  
536 Tanaka, Y.L., Uriu, K., Liu, Y., Morizako, N., et al. (2022). The SARS-CoV-2  
537 Lambda variant exhibits enhanced infectivity and immune resistance. *Cell Rep*  
538 38, 110218. 10.1016/j.celrep.2021.110218.  
539 Korber, B., Fischer, W.M., Gnanakaran, S., Yoon, H., Theiler, J., Abfalterer, W.,  
540 Hengartner, N., Giorgi, E.E., Bhattacharya, T., Foley, B., et al. (2020). Tracking  
541 changes in SARS-CoV-2 spike: evidence that D614G increases infectivity of the  
542 COVID-19 virus. *Cell* 182, 812-827. 10.1016/j.cell.2020.06.043.  
543 Li, H., and Durbin, R. (2009). Fast and accurate short read alignment with  
544 Burrows-Wheeler transform. *Bioinformatics* 25, 1754-1760.  
545 10.1093/bioinformatics/btp324.  
546 Li, H., Handsaker, B., Wysoker, A., Fennell, T., Ruan, J., Homer, N., Marth, G.,  
547 Abecasis, G., Durbin, R., and Genome Project Data Processing Subgroup  
548 (2009). The sequence alignment/map format and SAMtools. *Bioinformatics* 25,  
549 2078-2079. 10.1093/bioinformatics/btp352.  
550 Li, Q., Wu, J., Nie, J., Zhang, L., Hao, H., Liu, S., Zhao, C., Zhang, Q., Liu, H.,  
551 Nie, L., et al. (2020). The impact of mutations in SARS-CoV-2 spike on viral  
552 infectivity and antigenicity. *Cell* 182, 1284-1294 e1289.  
553 10.1016/j.cell.2020.07.012.  
554 Liu, L., Iketani, S., Guo, Y., Chan, J.F.-W., Wang, M., Liu, L., Luo, Y., Chu, H.,  
555 Huang, Y., Nair, M.S., et al. (2021). Striking antibody evasion manifested by the  
556 Omicron variant of SARS-CoV-2. *Nature*, doi:  
557 <https://doi.org/10.1038/d41586-41021-03826-41583>.  
558 Mannar, D., Saville, J.W., Zhu, X., Srivastava, S.S., Berezhuk, A.M., Tuttle, K.S.,  
559 Marquez, A.C., Sekirov, I., and Subramaniam, S. (2022). SARS-CoV-2 Omicron  
560 variant: Antibody evasion and cryo-EM structure of spike protein-ACE2 complex.  
561 *Science* 375, 760-764. 10.1126/science.abn7760.  
562 Martin, D.P., Murrell, B., Golden, M., Khoosal, A., and Muhire, B. (2015). RDP4:  
563 detection and analysis of recombination patterns in virus genomes. *Virus Evol* 1,

564 vev003. 10.1093/ve/vev003.

565 Martinez, C.R., and Iverson, B.L. (2012). Rethinking the term “pi-stacking”.

566 Chemical Science 3, 2191-2201.

567 Matsuyama, S., Nao, N., Shirato, K., Kawase, M., Saito, S., Takayama, I.,

568 Nagata, N., Sekizuka, T., Katoh, H., Kato, F., et al. (2020). Enhanced isolation of

569 SARS-CoV-2 by TMPRSS2-expressing cells. Proc Natl Acad Sci U S A 117,

570 7001-7003. 10.1073/pnas.2002589117.

571 Meng, B., Abdullahi, A., Ferreira, I.A.T.M., Goonawardane, N., Saito, A., Kimura,

572 I., Yamasoba, D., Gerber, P.P., Fatihi, S., Rathore, S., et al. (2022). Altered

573 TMPRSS2 usage by SARS-CoV-2 Omicron impacts tropism and fusogenicity.

574 Nature. 10.1038/s41586-022-04474-x.

575 Mlcochova, P., Kemp, S.A., Dhar, M.S., Papa, G., Meng, B., Ferreira, I., Datir, R.,

576 Collier, D.A., Albecka, A., Singh, S., et al. (2021). SARS-CoV-2 B.1.617.2 Delta

577 variant replication and immune evasion. Nature 599, 114-119.

578 10.1038/s41586-021-03944-y.

579 Motozono, C., Toyoda, M., Zahradnik, J., Saito, A., Nasser, H., Tan, T.S., Ngare,

580 I., Kimura, I., Uriu, K., Kosugi, Y., et al. (2021). SARS-CoV-2 spike L452R

581 variant evades cellular immunity and increases infectivity. Cell Host Microbe 29,

582 1124-1136. 10.1016/j.chom.2021.06.006.

583 National Institute for Communicable Diseases, S.A. (2021). “New COVID-19

584 variant detected in South Africa (November 25, 2021)”.

585 <https://www.nicd.ac.za/new-covid-19-variant-detected-in-south-africa/>.

586 Niwa, H., Yamamura, K., and Miyazaki, J. (1991). Efficient selection for

587 high-expression transfectants with a novel eukaryotic vector. Gene 108, 193-199.

588 10.1016/0378-1119(91)90434-d.

589 Ozono, S., Zhang, Y., Ode, H., Sano, K., Tan, T.S., Imai, K., Miyoshi, K.,

590 Kishigami, S., Ueno, T., Iwatani, Y., et al. (2021). SARS-CoV-2 D614G spike

591 mutation increases entry efficiency with enhanced ACE2-binding affinity. Nat

592 Commun 12, 848. 10.1038/s41467-021-21118-2.

593 Ozono, S., Zhang, Y., Tobiume, M., Kishigami, S., and Tokunaga, K. (2020).

594 Super-rapid quantitation of the production of HIV-1 harboring a luminescent

595 peptide tag. J Biol Chem 295, 13023-13030. 10.1074/jbc.RA120.013887.

596 Peleg, Y., and Unger, T. (2014). Application of the restriction-free (RF) cloning

597 for multicomponents assembly. Methods Mol Biol 1116, 73-87.

598 10.1007/978-1-62703-764-8\_6.

599 Planas, D., Saunders, N., Maes, P., Guivel-Benhassine, F., Planchais, C.,

600 Buchrieser, J., Bolland, W.-H., Porrot, F., Staropoli, I., Lemoine, F., et al. (2021).

601 Considerable escape of SARS-CoV-2 Omicron to antibody neutralization.

602 Nature, doi: <https://doi.org/10.1038/d41586-41021-03827-41582>.

603 Plante, J.A., Liu, Y., Liu, J., Xia, H., Johnson, B.A., Lokugamage, K.G., Zhang,

604 X., Muruato, A.E., Zou, J., Fontes-Garfias, C.R., et al. (2020). Spike mutation

605 D614G alters SARS-CoV-2 fitness. *Nature*. 10.1038/s41586-020-2895-3.  
606 Rambaut, A., Drummond, A.J., Xie, D., Baele, G., and Suchard, M.A. (2018).  
607 Posterior summarization in Bayesian phylogenetics using Tracer 1.7. *Syst Biol*  
608 67, 901-904. 10.1093/sysbio/syy032.  
609 Reed, L.J., and Muench, H. (1938). A simple method of estimating fifty percent  
610 endpoints. *Am J Hygiene* 27, 493-497.  
611 Rodriguez, F., Oliver, J.L., Marin, A., and Medina, J.R. (1990). The general  
612 stochastic model of nucleotide substitution. *J Theor Biol* 142, 485-501.  
613 10.1016/s0022-5193(05)80104-3.  
614 Saito, A., Irie, T., Suzuki, R., Maemura, T., Nasser, H., Uriu, K., Kosugi, Y.,  
615 Shirakawa, K., Sadamasu, K., Kimura, I., et al. (2022). Enhanced fusogenicity  
616 and pathogenicity of SARS-CoV-2 Delta P681R mutation. *Nature* 602, 300-306.  
617 10.1038/s41586-021-04266-9.  
618 Suchard, M.A., Lemey, P., Baele, G., Ayres, D.L., Drummond, A.J., and  
619 Rambaut, A. (2018). Bayesian phylogenetic and phylodynamic data integration  
620 using BEAST 1.10. *Virus Evol* 4, vey016. 10.1093/ve/vey016.  
621 Suzuki, R., Yamasoba, D., Kimura, I., Wang, L., Kishimoto, M., Ito, J., Morioka,  
622 Y., Nao, N., Nasser, H., Uriu, K., et al. (2022). Attenuated fusogenicity and  
623 pathogenicity of SARS-CoV-2 Omicron variant. *Nature*.  
624 10.1038/s41586-022-04462-1.  
625 Takashita, E., Kinoshita, N., Yamayoshi, S., Sakai-Tagawa, Y., Fujisaki, S., Ito,  
626 M., Iwatsuki-Horimoto, K., Chiba, S., Halfmann, P., Nagai, H., et al. (2022).  
627 Efficacy of antibodies and antiviral drugs against Covid-19 Omicron variant. *N*  
628 *Engl J Med*. 10.1056/NEJMc2119407.  
629 Torii, S., Ono, C., Suzuki, R., Morioka, Y., Anzai, I., Fauzyah, Y., Maeda, Y.,  
630 Kamitani, W., Fukuhara, T., and Matsuura, Y. (2021). Establishment of a reverse  
631 genetics system for SARS-CoV-2 using circular polymerase extension reaction.  
632 *Cell Rep* 35, 109014.  
633 Uriu, K., Cardenas, P., Munoz, E., Barragan, V., Kosugi, Y., Shirakawa, K.,  
634 Takaori-Kondo, A., Sato, K., Ecuador-Covid19 Consortium, and The Genotype  
635 to Phenotype Japan (G2P-Japan) Consortium (2022). Characterization of the  
636 immune resistance of SARS-CoV-2 Mu variant and the robust immunity induced  
637 by Mu infection. *J Infect Dis*. 10.1093/infdis/jiac053.  
638 Uriu, K., Kimura, I., Shirakawa, K., Takaori-Kondo, A., Nakada, T.A., Kaneda, A.,  
639 Nakagawa, S., Sato, K., and The Genotype to Phenotype Japan (G2P-Japan)  
640 Consortium (2021). Neutralization of the SARS-CoV-2 Mu variant by  
641 convalescent and vaccine serum. *N Engl J Med* 385, 2397-2399.  
642 10.1056/NEJMc2114706.  
643 VanBlargan, L.A., Errico, J.M., Halfmann, P.J., Zost, S.J., Crowe, J.E., Jr.,  
644 Purcell, L.A., Kawaoka, Y., Corti, D., Fremont, D.H., and Diamond, M.S. (2022).  
645 An infectious SARS-CoV-2 B.1.1.529 Omicron virus escapes neutralization by

646 therapeutic monoclonal antibodies. *Nat Med.* 10.1038/s41591-021-01678-y.  
647 WHO (2022). “Tracking SARS-CoV-2 variants (March 22, 2022)”.  
648 <https://www.who.int/en/activities/tracking-SARS-CoV-2-variants/>.  
649 Wu, F., Zhao, S., Yu, B., Chen, Y.M., Wang, W., Song, Z.G., Hu, Y., Tao, Z.W.,  
650 Tian, J.H., Pei, Y.Y., et al. (2020). A new coronavirus associated with human  
651 respiratory disease in China. *Nature* 579, 265-269. 10.1038/s41586-020-2008-3.  
652 Yamasoba, D., Kimura, I., Nasser, H., Morioka, Y., Nao, N., Ito, J., Uriu, K.,  
653 Tsuda, M., Zahradnik, J., Shirakawa, K., et al. (2022). Virological characteristics  
654 of SARS-CoV-2 BA.2 variant. *BioRxiv*, doi:  
655 <https://doi.org/10.1101/2022.1102.1114.480335>.  
656 Yang, Z. (1996). Among-site rate variation and its impact on phylogenetic  
657 analyses. *Trends Ecol Evol* 11, 367-372. 10.1016/0169-5347(96)10041-0.  
658 Yurkovetskiy, L., Wang, X., Pascal, K.E., Tomkins-Tinch, C., Nyalile, T.P., Wang,  
659 Y., Baum, A., Diehl, W.E., Dauphin, A., Carbone, C., et al. (2020). Structural and  
660 functional analysis of the D614G SARS-CoV-2 spike protein variant. *Cell* 183,  
661 739-751 e738. 10.1016/j.cell.2020.09.032.  
662 Zahradnik, J., Marciano, S., Shemesh, M., Zoler, E., Harari, D., Chiaravalli, J.,  
663 Meyer, B., Rudich, Y., Li, C., Marton, I., et al. (2021). SARS-CoV-2 variant  
664 prediction and antiviral drug design are enabled by RBD in vitro evolution. *Nat*  
665 *Microbiol* 6, 1188-1198. 10.1038/s41564-021-00954-4.  
666 Zhang, J., Cai, Y., Xiao, T., Lu, J., Peng, H., Sterling, S.M., Walsh, R.M., Jr.,  
667 Rits-Volloch, S., Zhu, H., Woosley, A.N., et al. (2021). Structural impact on  
668 SARS-CoV-2 spike protein by D614G substitution. *Science* 372, 525-530.  
669 10.1126/science.abf2303.  
670  
671



## 672 **Methods**

### 673 **Ethics statement**

674 All experiments with hamsters were performed in accordance with the Science  
675 Council of Japan's Guidelines for the Proper Conduct of Animal Experiments.  
676 The protocols were approved by the Institutional Animal Care and Use  
677 Committee of National University Corporation Hokkaido University (approval ID:  
678 20-0060). All protocols involving specimens from human subjects recruited at  
679 Kyoto University and Kuramochi Clinic Interpark were reviewed and approved by  
680 the Institutional Review Boards of Kyoto University (approval ID: G1309) and  
681 Kuramochi Clinic Interpark (approval ID: G2021-004). All human subjects  
682 provided written informed consent. All protocols for the use of human specimens  
683 were reviewed and approved by the Institutional Review Boards of The Institute  
684 of Medical Science, The University of Tokyo (approval IDs: 2021-1-0416 and  
685 2021-18-0617), Kyoto University (approval ID: G0697), Kumamoto University  
686 (approval IDs: 2066 and 2074), and University of Miyazaki (approval ID:  
687 O-1021).

688

### 689 **Human serum collection**

690 Vaccine sera were collected from eleven vaccinees four weeks after their  
691 second vaccination with the BNT162b2 (Pfizer/BioNTech) vaccine (average age:  
692 35, range: 29-56, 18% male) and sixteen vaccinees four weeks after their  
693 second mRNA-1273 (Moderna) vaccine (average age: 27, range: 20-47, 38%  
694 male).

695 Convalescent sera were collected from vaccine-naïve individuals who  
696 had been infected with the Delta variant (n=10; average age: 47, range: 22-63,  
697 70% male). To identify the SARS-CoV-2 variants infecting patients, saliva was  
698 collected from COVID-19 patients during infection onset, and RNA was  
699 extracted using a QIAamp viral RNA mini kit (Qiagen, Cat# 52906) according to  
700 the manufacturer's protocol. To identify the Delta variants, viral genome  
701 sequencing was performed as previously described ([Meng et al., 2022](#)). For  
702 details, see the "Viral genome sequencing" section below. Sera collected from  
703 twelve convalescents during the early pandemic (until May 2020) (average age:  
704 71, range: 52-92, 8% male) were purchased from RayBiotech. Sera were  
705 inactivated at 56°C for 30 min and stored at -80°C until use. The details of the  
706 sera used in this study are summarized in **Table S1**.

707

### 708 **Hamster serum collection**

709 Animal experiments were performed as previously described ([Saito et al., 2022](#);  
710 [Suzuki et al., 2022](#); [Yamasoba et al., 2022](#)). Syrian hamsters (male, 4 weeks  
711 old) were purchased from Japan SLC Inc. (Shizuoka, Japan). For the virus  
712 infection experiments, hamsters were anaesthetized by intramuscular injection

of a mixture of either 0.15 mg/kg medetomidine hydrochloride (Domitor<sup>®</sup>, Nippon Zenyaku Kogyo), 2.0 mg/kg midazolam (FUJIFILM Wako Chemicals, Cat# 135-13791) and 2.5 mg/kg butorphanol (Vetorphale<sup>®</sup>, Meiji Seika Pharma), or 0.15 mg/kg medetomidine butorphanol. The chimeric recombinant SARS-CoV-2 (rB.1.1 S-GFP and rBA.1 S-GFP) (10,000 TCID<sub>50</sub> in 100 µl) were intranasally inoculated under anesthesia (Yamasoba *et al.*, 2022). Sera of infected hamsters were collected at 16 days postinfection (d.p.i.) using cardiac puncture under anesthesia with isoflurane and stored at −80°C until use.

721

## 722 Cell culture

HEK293T cells (a human embryonic kidney cell line; ATCC, CRL-3216), HEK293 cells (a human embryonic kidney cell line; ATCC CRL-1573), and HOS-ACE2/TMPRSS2 cells, HOS cells stably expressing human ACE2 and TMPRSS2 (Ferreira *et al.*, 2021; Ozono *et al.*, 2021) were maintained in DMEM (high glucose) (Sigma-Aldrich, Cat# 6429-500ML) containing 10% fetal bovine serum (FBS) and 1% penicillin-streptomycin (PS). HEK293-C34 cells, *IFNAR1* KO HEK293 cells expressing human ACE2 and TMPRSS2 by doxycycline treatment (Torii *et al.*, 2021), were maintained in Dulbecco's modified Eagle's medium (high glucose) (Sigma-Aldrich, Cat# R8758-500ML) containing 10% FBS, 10 µg/ml blasticidin (InvivoGen, Cat# ant-bl-1) and 1% PS.

733

VeroE6/TMPRSS2 cells (VeroE6 cells stably expressing human TMPRSS2; JCRB1819) (Matsuyama *et al.*, 2020) were maintained in DMEM (low glucose) (Wako, Cat# 041-29775) containing 10% FBS, G418 (1 mg/ml; Nacalai Tesque, Cat# G8168-10ML) and 1% PS. Expi293F cells (Thermo Fisher Scientific, Cat# A14527) were maintained in Expi293 expression medium (Thermo Fisher Scientific, Cat# A1435101).

740

## 741 METHOD DETAILS

### 742 Viral genome sequencing

Viral genome sequencing was performed as previously described (Motozono *et al.*, 2021; Saito *et al.*, 2022; Suzuki *et al.*, 2022; Yamasoba *et al.*, 2022) with some modifications. Briefly, the virus sequences were verified by viral RNA-sequencing analysis. Viral RNA was extracted using a QIAamp viral RNA mini kit (Qiagen, Cat# 52906). The sequencing library employed for total RNA sequencing was prepared using the NEB Next Ultra RNA Library Prep Kit for Illumina (New England Biolabs, Cat# E7530). Paired-end 76-bp sequencing was performed using a MiSeq system (Illumina) with MiSeq reagent kit v3 (Illumina, Cat# MS-102-3001). Sequencing reads were trimmed using fastp v0.21.0 (Chen *et al.*, 2018) and subsequently mapped to the viral genome sequences of a lineage A isolate (strain WK-521; GISAID ID: EPI\_ISL\_408667) (Matsuyama *et*



754 [al., 2020](#)) using BWA-MEM v0.7.17 ([Li and Durbin, 2009](#)). Variant calling,  
755 filtering, and annotation were performed using SAMtools v1.9 ([Li et al., 2009](#))  
756 and snpEff v5.0e ([Cingolani et al., 2012](#)).

757

## 758 **Molecular phylogenetic analyses**

759 The SARS-CoV-2 genomes and annotation information used in this study were  
760 downloaded from the GISAID EpiCoV database (<https://www.gisaid.org/>) on  
761 January 8, 2022 (6,780,682 sequences). A total of 204,375 Omicron BA.1  
762 variants were obtained, which included 1,074 B.1.1.529 variants because the  
763 B.1.1.529 lineage was recategorized as BA.1 as of February 24, 2022  
764 ([https://cov-lineages.org/lineage\\_list.html](https://cov-lineages.org/lineage_list.html)). For each sequence, we counted the  
765 number of undetermined nucleotides (such as N, Y, W) for whole genomes as  
766 well as S genes and obtained 40,739 sequences with fewer than 1,000  
767 undetermined nucleotides in the genome and fewer than 10 undetermined  
768 nucleotides in the S-coding region. We then obtained BA.1 variant genomes that  
769 met the following criteria: 1) genomes were isolated from humans; 2) genomes  
770 did not contain any undetermined nucleotides in genomic regions corresponding  
771 to amino acid positions 371-375 in the S protein; 3) genomes were sampled from  
772 September 2021 to November 2021; and 4) genomes did not contain any of the  
773 3 amino acid replacements in the S protein. We then selected 12 genomes and  
774 randomly selected 100 genomes that met criteria 1 and 2. By removing genomes  
775 that include possible recombination events by using RDP4 v4.101 ([Martin et al.,](#)  
776 [2015](#)), 48 Omicron genomes were obtained.

777 The 48 Omicron genomes with two outgroup genomes  
778 EPI\_ISL\_402125 (strain Wuhan-Hu-1, B lineage) and EPI\_ISL\_406862 (B.1  
779 lineage; one of the earliest sequences carrying the S D614G mutation) were  
780 aligned using FFT-NS-1 in MAFFT suite v7.407 ([Katoh and Standley, 2013](#)). We  
781 then deleted gapped regions in the 5' and 3' regions. BEAST v1.10.4 ([Suchard](#)  
782 [et al., 2018](#)) was used to construct a timetree under an exponential growth  
783 coalescent model using a strict molecular clock. The GTR model with the four  
784 categories of discrete gamma rate variation was used as a nucleotide  
785 substitution model ([Rodriguez et al., 1990](#); [Yang, 1996](#)). We ran Markov Chain  
786 Monte Carlo (MCMC) procedures with a  $1 \times 10^8$  chain length for all calculations,  
787 discarding the first 10% as burn-in and sampling every 10,000 replicates. The  
788 effective sample size for all run was confirmed to be larger than 200. FigTree  
789 v1.4.4 (<http://tree.bio.ed.ac.uk/software/figtree/>) was used to show the tree. To  
790 further determine the population history of the Omicron genomes, we generated  
791 a Bayesian skyline plot using the same model ( $2 \times 10^8$  chain length for MCMC)  
792 and summarized the results using Tracer v1.7.1 ([Rambaut et al., 2018](#)).

793

## 794 **Plasmid construction**

Plasmids expressing the codon-optimized SARS-CoV-2 S proteins of B.1 (the parental D614G-bearing variant), Delta (B.1.617.2) and Omicron (BA.1 lineage) variants were prepared in our previous studies (Ferreira *et al.*, 2021; Kimura *et al.*, 2022; Motozono *et al.*, 2021; Saito *et al.*, 2022; Suzuki *et al.*, 2022; Uriu *et al.*, 2022; Uriu *et al.*, 2021; Yamasoba *et al.*, 2022). Plasmids expressing a series of SAR-CoV-2 S mutants were generated by site-directed overlap extension PCR using the primers listed in **Table S3**. The resulting PCR fragment was digested with KpnI and NotI and inserted into the corresponding site of the pCAGGS vector (Niwa *et al.*, 1991). Nucleotide sequences were determined by DNA sequencing services (Eurofins), and the sequence data were analyzed by Sequencher v5.1 software (Gene Codes Corporation).

806

### 807 **Pseudovirus assay**

Pseudovirus assay was performed as previously described (Ferreira *et al.*, 2021; Kimura *et al.*, 2022; Motozono *et al.*, 2021; Saito *et al.*, 2022; Suzuki *et al.*, 2022; Uriu *et al.*, 2022; Uriu *et al.*, 2021; Yamasoba *et al.*, 2022). Briefly, lentivirus (HIV-1)-based, luciferase-expressing reporter viruses were pseudotyped with the SARS-CoV-2 spikes. HEK293T cells (500,000 cells) were cotransfected with 800 ng psPAX2-IN/HiBiT (Ozono *et al.*, 2020), 800 ng pWPI-Luc2 (Ozono *et al.*, 2020), and 400 ng plasmids expressing parental S or its derivatives using TransIT-293 Transfection Reagent (Takara, Cat# MIR2700) or or PEI Max (Polysciences, Cat# 24765-1) according to the manufacturer's protocol. Two days posttransfection, the culture supernatants were harvested, and the pseudoviruses were stored at -80°C until use. The same amount of pseudoviruses (normalized to the HiBiT value, which indicates the amount of p24 HIV-1 antigen) was inoculated into HOS-ACE2/TMPRSS2. At two days postinfection, the infected cells were lysed with a Bright-Glo Luciferase Assay System (Promega, cat# E2620) or a One-Glo luciferase assay system (Promega, cat# E6130) and the luminescent signal was measured using a GloMax Explorer Multimode Microplate Reader (Promega) or a CentroXS3 plate reader (Berthold Technologies).

826

### 827 **Western blot**

Western blot was performed as previously described (Saito *et al.*, 2022; Suzuki *et al.*, 2022; Yamasoba *et al.*, 2022). For the blot, the HEK293 cells cotransfected with the S expression plasmids and HIV-1-based pseudovirus producing plasmids (see “Pseudovirus assay” section above) or the HEK293 cells transfected with the S expression plasmids were used. To quantify the level of the cleaved S2 protein in the cells, the harvested cells were washed and lysed in lysis buffer [25 mM HEPES (pH 7.2), 20% glycerol, 125 mM NaCl, 1% Nonidet P40 substitute (Nacalai Tesque, Cat# 18558-54), protease inhibitor cocktail

(Nacalai Tesque, Cat# 03969-21)]. After quantification of total protein by protein assay dye (Bio-Rad, Cat# 5000006), lysates were diluted with 2 × sample buffer [100 mM Tris-HCl (pH 6.8), 4% SDS, 12% β-mercaptoethanol, 20% glycerol, 0.05% bromophenol blue] and boiled for 10 m. Then, 10 μl samples (50 μg of total protein) were subjected to Western blot. To quantify the level of the S2 protein in the virions, 900 μl culture medium containing the pseudoviruses was layered onto 500 μl 20% sucrose in PBS and centrifuged at 20,000 g for 2 h at 4°C. Pelleted virions were resuspended in 1× NuPAGE LDS sample buffer (Thermo Fisher Scientific, Cat# NP0007) containing 2% β-mercaptoethanol and incubated at 70°C for 10 m. For protein detection, the following antibodies were used: mouse anti-SARS-CoV-2 S monoclonal antibody (clone 1A9, GeneTex, Cat# GTX632604, 1:10,000), mouse anti-HIV-1 p24 monoclonal antibody (183-H12-5C, obtained from the HIV Reagent Program, NIH, Cat# ARP-3537, 1:2,000), rabbit anti-beta actin (ACTB) monoclonal antibody (clone 13E5, Cell Signalling, Cat# 4970, 1:5,000), mouse anti-tubulin (TUBA) monoclonal antibody (clone DM1A, Sigma-Aldrich, Cat# T9026, 1:10,000), horseradish peroxidase (HRP)-conjugated horse anti-mouse IgG antibody (Cell Signaling, Cat# 7076S, 1:2,000), HRP-conjugated donkey anti-rabbit IgG polyclonal antibody (Jackson ImmunoResearch, Cat# 711-035-152, 1:10,000) and HRP-conjugated donkey anti-mouse IgG polyclonal antibody (Jackson ImmunoResearch, Cat# 715-035-150, 1:10,000). Chemiluminescence was detected using SuperSignal West Femto Maximum Sensitivity Substrate (Thermo Fisher Scientific, Cat# 34095), SuperSignal West Atto Ultimate Sensitivity Substrate (Thermo Fisher Scientific, Cat# A38554) or Western BLoT Ultra Sensitive HRP Substrate (Takara, Cat# T7104A) according to the manufacturer's instruction. Bands were visualized using an Amersham Imager 600 (GE Healthcare) or iBright FL1500 Imaging System (Thermo Fisher Scientific), and the band intensity was quantified using Image Studio Lite v5.2 (LI-COR Biosciences) or Fiji software v2.2.0 (ImageJ).

## **SARS-CoV-2 S-based fusion assay**

SARS-CoV-2 S-based fusion assay was performed as previously described (Motozono *et al.*, 2021; Saito *et al.*, 2022; Suzuki *et al.*, 2022; Yamasoba *et al.*, 2022). This assay utilizes a dual split protein (DSP) encoding *Renilla* luciferase and *GFP* genes; the respective split proteins, DSP<sub>8-11</sub> and DSP<sub>1-7</sub>, are expressed in effector and target cells by transfection. Briefly, on day 1, effector cells (i.e., S-expressing cells) and target cells (see below) were prepared at a density of 0.6–0.8 × 10<sup>6</sup> cells in a 6-well plate. To prepare effector cells, HEK293 cells were cotransfected with the S expression plasmids (400 ng) and pDSP<sub>8-11</sub> (400 ng) using TransIT-LT1 (Takara, Cat# MIR2300). To prepare target cells, HEK293 cells were cotransfected with pC-ACE2 (200 ng) and pDSP<sub>1-7</sub> (400 ng).

Target HEK293 cells in selected wells were cotransfected with pC-TMPRSS2 (40 ng) in addition to the plasmids above. HEK293-ACE2 cells and HEK293-ACE2/TMPRSS2 cells were transfected with pDSP<sub>1-7</sub> (400ng). On day 3 (24 h posttransfection), 16,000 effector cells were detached and reseeded into 96-well black plates (PerkinElmer, Cat# 6005225), and target HEK293 cells were reseeded at a density of 1,000,000 cells/2 ml/well in 6-well plates. On day 4 (48 h posttransfection), target cells were incubated with EnduRen live cell substrate (Promega, Cat# E6481) at 37°C for 3 h and then detached, and 32,000 target cells were added to a 96-well plate with effector cells. *Renilla* luciferase activity was measured at the indicated time points using Centro XS3 LB960 (Berthold Technologies). To measure the surface expression level of S protein, effector cells were stained with rabbit anti-SARS-CoV-2 S S1/S2 polyclonal antibody (Thermo Fisher Scientific, Cat# PA5-112048, 1:100). Normal rabbit IgG (SouthernBiotech, Cat# 0111-01, 1:100) was used as negative controls, and APC-conjugated goat anti-rabbit IgG polyclonal antibody (Jackson ImmunoResearch, Cat# 111-136-144, 1:50) was used as a secondary antibody. Surface expression level of S protein was measured using FACS Canto II (BD Biosciences) and the data were analyzed using FlowJo software v10.7.1 (BD Biosciences). To calculate fusion activity, *Renilla* luciferase activity was normalized to the MFI of surface S proteins. The normalized value (i.e., *Renilla* luciferase activity per the surface S MFI) is shown as fusion activity.

### SARS-CoV-2 reverse genetics

Recombinant SARS-CoV-2 was generated by circular polymerase extension reaction (CPER) as previously described (Motozono *et al.*, 2021; Saito *et al.*, 2022; Torii *et al.*, 2021; Yamasoba *et al.*, 2022). In brief, 9 DNA fragments encoding the partial genome of SARS-CoV-2 (strain WK-521, PANGO lineage A; GISAID ID: EPI\_ISL\_408667) (Matsuyama *et al.*, 2020) were prepared by PCR using PrimeSTAR GXL DNA polymerase (Takara, Cat# R050A). A linker fragment encoding hepatitis delta virus ribozyme, bovine growth hormone poly A signal and cytomegalovirus promoter was also prepared by PCR. The corresponding SARS-CoV-2 genomic region and the PCR templates and primers used for this procedure are summarized in **Table S3**. The 10 obtained DNA fragments were mixed and used for CPER (Torii *et al.*, 2021). To prepare GFP-expressing replication-competent recombinant SARS-CoV-2, we used fragment 9, in which the *GFP* gene was inserted in the *ORF7a* frame, instead of the authentic F9 fragment (**Table S3**) (Torii *et al.*, 2021).

To generate chimeric recombinant SARS-CoV-2 (**Figures 1G and 5A**), mutations were inserted in fragment 8 by site-directed overlap extension PCR or the GENEART site-directed mutagenesis system (Thermo Fisher Scientific,

917 Cat# A13312) according to the manufacturer's protocol with the primers listed in  
918 **Table S3**. Recombinant SARS-CoV-2 that bears B.1 S [rB.1 S-GFP (virus I)] or  
919 Omicron S [rOmicron S-GFP (virus II)] was prepared in our previous studies  
920 (Saito *et al.*, 2022; Yamasoba *et al.*, 2022). Nucleotide sequences were  
921 determined by a DNA sequencing service (Fasmac), and the sequence data  
922 were analyzed by Sequencher v5.1 software (Gene Codes Corporation).

923 To produce chimeric recombinant SARS-CoV-2, the CPER products  
924 were transfected into HEK293-C34 cells using TransIT-LT1 (Takara, Cat#  
925 MIR2300) according to the manufacturer's protocol. At 1 d posttransfection, the  
926 culture medium was replaced with Dulbecco's modified Eagle's medium (high  
927 glucose) (Sigma-Aldrich, Cat# R8758-500ML) containing 2% FCS, 1% PS and  
928 doxycycline (1 µg/ml; Takara, Cat# 1311N). At 7 d posttransfection, the culture  
929 medium was harvested and centrifuged, and the supernatants were collected as  
930 the seed virus. To remove the CPER products (i.e., SARS-CoV-2-related DNA),  
931 1 ml of the seed virus was treated with 2 µl TURBO DNase (Thermo Fisher  
932 Scientific, Cat# AM2238) and incubated at 37°C for 1 h. Complete removal of the  
933 CPER products (i.e., SARS-CoV-2-related DNA) from the seed virus was  
934 verified by PCR. The working virus stock was prepared from the seed virus as  
935 described below (see "SARS-CoV-2 preparation and titration" section).

### 936 **SARS-CoV-2 preparation and titration**

937 The working virus stocks of chimeric recombinant SARS-CoV-2 were prepared  
938 and titrated as previously described (Motozono *et al.*, 2021; Saito *et al.*, 2022;  
939 Suzuki *et al.*, 2022; Torii *et al.*, 2021; Yamasoba *et al.*, 2022). In brief, 20 µl of  
940 the seed virus was inoculated into VeroE6/TMPRSS2 cells (5,000,000 cells in a  
941 T-75 flask). One hour post infection (h.p.i.), the culture medium was replaced  
942 with DMEM (low glucose) (Wako, Cat# 041-29775) containing 2% FBS and 1%  
943 PS. At 3 d.p.i., the culture medium was harvested and centrifuged, and the  
944 supernatants were collected as the working virus stock.

945 The titer of the prepared working virus was measured as the 50%  
946 tissue culture infectious dose (TCID<sub>50</sub>). Briefly, one day before infection,  
947 VeroE6/TMPRSS2 cells (10,000 cells) were seeded into a 96-well plate. Serially  
948 diluted virus stocks were inoculated into the cells and incubated at 37°C for 4 d.  
949 The cells were observed under microscopy to judge the CPE appearance. The  
950 value of TCID<sub>50</sub>/ml was calculated with the Reed–Muench method (Reed and  
951 Muench, 1938).

952 To verify the sequence of chimeric recombinant SARS-CoV-2, viral  
953 RNA was extracted from the working viruses using a QIAamp viral RNA mini kit  
954 (Qiagen, Cat# 52906) and viral genome sequence was analyzed as described  
955 above (see "Viral genome sequencing" section above). In brief, the viral  
956 sequences of GFP-encoding recombinant SARS-CoV-2 (strain WK-521; GSIAD  
957



958 ID: EPI\_ISL\_408667) ([Matsuyama et al., 2020](#); [Torii et al., 2021](#)) that harbor the  
959 S genes of respective variants were used for the reference. Information on the  
960 unexpected mutations detected is summarized in **Table S4**, and the raw data  
961 are deposited in Gene Expression Omnibus (accession number: GSE196649  
962 and xxxx).

963

# **SARS-CoV-2 infection**

964 SARS-CoV-2 infection was performed as previously described ([Meng et al.,](#)  
965 [2022](#); [Motozono et al., 2021](#); [Saito et al., 2022](#); [Suzuki et al., 2022](#); [Yamasoba et](#)  
966 [al., 2022](#)). Briefly, 1 d before infection, VeroE6/TMPRSS2 cells (10,000 cells)  
967 were seeded into a 96-well plate. SARS-CoV-2 (100 TCID<sub>50</sub>, m.o.i. 0.01) was  
968 inoculated and incubated at 37°C for 1 h. The infected cells were washed, and  
969 180 µl of culture medium was added. The culture supernatant (10 µl) was  
970 harvested at the indicated timepoints and used for RT-qPCR to quantify the viral  
971 RNA copy number (see “RT-qPCR” section below).

973

# **RT-qPCR**

974 RT-qPCR was performed as previously described ([Meng et al., 2022](#); [Motozono](#)  
975 [et al., 2021](#); [Saito et al., 2022](#); [Suzuki et al., 2022](#); [Yamasoba et al., 2022](#)).  
976 Briefly, 5 µl of culture supernatant was mixed with 5 µl of 2 × RNA lysis buffer  
977 [2% Triton X-100, 50 mM KCl, 100 mM Tris-HCl (pH 7.4), 40% glycerol, 0.8 U/µl  
978 recombinant RNase inhibitor (Takara, Cat# 2313B)] and incubated at room  
979 temperature for 10 min. RNase-free water (90 µl) was added, and the diluted  
980 sample (2.5 µl) was used as the template for real-time RT-PCR performed  
981 according to the manufacturer’s protocol using the One Step TB Green  
982 PrimeScript PLUS RT-PCR kit (Takara, Cat# RR096A) and the following  
983 primers: Forward N, 5'-AGC CTC TTC TCG TTC CTC ATC AC-3'; and Reverse  
984 N, 5'-CCG CCA TTG CCA GCC ATT C-3'. The viral RNA copy number was  
985 standardized with a SARS-CoV-2 direct detection RT-qPCR kit (Takara, Cat#  
986 RC300A). Fluorescent signals were acquired using QuantStudio 3 Real-Time  
987 PCR system (Thermo Fisher Scientific), CFX Connect Real-Time PCR Detection  
988 system (Bio-Rad), Eco Real-Time PCR System (Illumina), qTOWER3 G  
989 Real-Time System (Analytik Jena) or 7500 Real-Time PCR System (Thermo  
990 Fisher Scientific).

992

# **Fluorescence microscopy**

994 Fluorescence microscopy was performed as previously described ([Saito et al.,](#)  
995 [2022](#); [Yamasoba et al., 2022](#)). Briefly, 1 d before infection, VeroE6/TMPRSS2  
996 cells (10,000 cells) were seeded into 96-well, glass bottom, black plates and  
997 infected with SARS-CoV-2 (100 TCID<sub>50</sub>, m.o.i. 0.01). At 24, 48, and 72 h.p.i.,  
998 GFP fluorescence was observed under an All-in-One Fluorescence Microscope

999 BZ-X800 (Keyence) in living cells, and a 13-square-millimeter area of each  
1000 sample was scanned. under the same parameters. Images were reconstructed  
1001 using an BZ-X800 analyzer software (Keyence), and the area and the  
1002 fluorescent intensity of the GFP-positive cells was measured using this software.

### 1003 1004 **Plaque assay**

1005 Plaque assay was performed as previously described ([Motozono et al., 2021](#);  
1006 [Saito et al., 2022](#); [Suzuki et al., 2022](#); [Yamasoba et al., 2022](#)). Briefly, 1 d before  
1007 infection, VeroE6/TMPRSS2 cells (100,000 cells) were seeded into a 24-well  
1008 plate and infected with SARS-CoV-2 (1, 10, 100 and 1,000 TCID<sub>50</sub>) at 37°C for 2  
1009 h. Mounting solution containing 3% FBS and 1.5% carboxymethyl cellulose  
1010 (Wako, Cat# 039-01335) was overlaid, followed by incubation at 37°C. At 3 d.p.i.,  
1011 the culture medium was removed, and the cells were washed with PBS three  
1012 times and fixed with 4% paraformaldehyde phosphate (Nacalai Tesque, Cat#  
1013 09154-85). The fixed cells were washed with tap water, dried, and stained with  
1014 staining solution [0.1% methylene blue (Nacalai Tesque, Cat# 22412-14) in  
1015 water] for 30 m. The stained cells were washed with tap water and dried, and the  
1016 size of plaques was measured using Adobe Photoshop 2021 v22.4.1 (Adobe).

### 1017 1018 **Neutralization assay**

1019 Neutralization assay was performed as previously described ([Ferreira et al.,](#)  
1020 [2021](#); [Kimura et al., 2022](#); [Mlcochova et al., 2021](#); [Saito et al., 2022](#); [Uriu et al.,](#)  
1021 [2022](#); [Uriu et al., 2021](#); [Yamasoba et al., 2022](#)). Briefly, pseudoviruses were  
1022 prepared as described above (see “Pseudovirus assay” section). For the  
1023 neutralization assay, the SARS-CoV-2 S pseudoviruses (counting ~20,000  
1024 relative light units) were incubated with serially diluted (40-fold or 120-fold to  
1025 29,160-fold dilution at the final concentration) heat-inactivated sera at 37°C for 1  
1026 h. Pseudoviruses without sera were included as controls. Then, an 80 µl mixture  
1027 of pseudovirus and serum/antibody was added to HOS-ACE2/TMPRSS2 cells  
1028 (10,000 cells/50 µl) in a 96-well white plate. At 2 d.p.i., pseudovirus infectivity  
1029 was measured as described above (see “Pseudovirus assay” section). The  
1030 assay of each serum was performed in triplicate, and the 50% neutralization titer  
1031 (NT50) was calculated using Prism 9 (GraphPad Software).

### 1032 1033 **Protein structure**

1034 All protein structural analyses were performed using the PyMOL molecular  
1035 graphics system v2.5.0 (Schrödinger). The crystal structures of SARS-CoV-2  
1036 D614G (B.1 lineage) S (PDB: 7KRQ) ([Zhang et al., 2021](#)) and Omicron S (PDB:  
1037 7T9J) ([Mannar et al., 2022](#)) were used. To predict inter-subunit interaction of the  
1038 Omicron S trimer, each subunit of the D614G S trimer was replaced with the  
1039 Omicron S monomer([Mannar et al., 2022](#)). The distance between F375 and



1040 H505 was measured using the PyMOL molecular graphics system v2.5.0  
1041 (Schrödinger).

1042

### 1043 **Yeast surface display**

1044 Yeast surface display was performed as previously described ([Dejnirattisai et al., 2022](#); [Kimura et al., 2022](#); [Motozono et al., 2021](#); [Yamasoba et al., 2022](#); [Zahradnik et al., 2021](#)). Briefly, the carboxypeptidase domain of human ACE2  
1045 (residues 18-740) was expressed in Expi293F cells and purified by a 5-ml  
1046 HisTrap Fast Flow column (Cytiva, Cat# 17-5255-01) and Superdex 200 16/600  
1047 (Cytiva, Cat# 28-9893-35) using an ÄKTA pure chromatography system (Cytiva),  
1048 and the purified soluble ACE2 was labelled with CF640R (Biotium, Cat# 92108).  
1049 Protein quality was verified using a Tycho NT.6 system (NanoTemper) and  
1050 ACE2 activity assay kit (Sensolyte, Cat# AS-72086).  
1051

1052 An enhanced yeast display platform for SARS-CoV-2 S RBD [wild-type  
1053 (B.1.1), residues 336-528] yeast surface expression was established using  
1054 *Saccharomyces cerevisiae* EBY100 strain and pJYDC1 plasmid (Addgene, Cat#  
1055 162458) as previously described ([Dejnirattisai et al., 2022](#); [Kimura et al., 2022](#); [Motozono et al., 2021](#); [Yamasoba et al., 2022](#); [Zahradnik et al., 2021](#)). To  
1056 prepare a series of SARS-CoV-2 S RBD mutants, the site-directed mutagenesis  
1057 was performed using the KAPA HiFi HotStart ReadyMix kit (Roche, Cat#  
1058 KK2601) by restriction enzyme-free cloning procedure ([Peleg and Unger, 2014](#)).  
1059 Primers for mutagenesis are listed in **Table S3**.  
1060

1061 The binding affinities of SARS-CoV-2 S RBDs to human ACE2 were  
1062 determined by flow cytometry titration experiments. The CF640R-labelled ACE2  
1063 at 12–14 different concentrations (200 nM to 13 pM in PBS supplemented with  
1064 bovine serum albumin at 1 g/l) per measurement were incubated with expressed  
1065 yeast aliquots and 10 nM bilirubin (Sigma-Aldrich, Cat# 14370-1G) and analyzed  
1066 by using FACS S3e Cell Sorter device (Bio-Rad). The background binding  
1067 subtracted fluorescent signal was fitted to a standard noncooperative Hill  
1068 equation by nonlinear least-squares regression using Python v3.7  
1069 (<https://www.python.org>) as previously described ([Zahradnik et al., 2021](#)).  
1070

1071

### 1072 **QUANTIFICATION AND STATISTICAL ANALYSIS**

1073 In the single timepoint experiments, statistical significance was tested using a  
1074 two-sided Student's *t* test (**Figures 1B, 1E, 3B, 4B, 4E, 6D and 6E**), a two-sided  
1075 paired *t* test (**Figures 1D, 4D, 6B and 6C**), a two-sided Mann–Whitney *U* test  
1076 (**Figures 1J, 1K, 5D, 5E**), or a two-sided Wilcoxon signed-rank test (**Figure 2**).  
1077 The tests above were performed using Prism 9 software v9.1.1 (GraphPad  
1078 Software).

1079 In the time-course experiments (**Figures 1F, 1H, 1I, 4F, 5B, 5C, 6F,**  
1080 **and 6G**), a multiple regression analysis including experimental conditions (i.e.,

1081 the types of infected viruses) as explanatory variables and timepoints as  
 1082 qualitative control variables was performed to evaluate the difference between  
 1083 experimental conditions thorough all timepoints. *P* value was calculated by a  
 1084 two-sided Wald test. Subsequently, familywise error rates (FWERs) were  
 1085 calculated by the Holm method. These analyses were performed in R v4.1.2  
 1086 (<https://www.r-project.org/>).

1087 In **Figures 1F, 1J, 6C, 6D and S1A**, assays were performed in  
 1088 triplicate. Photographs shown are the representatives of >18 fields of view taken  
 1089 for each sample.

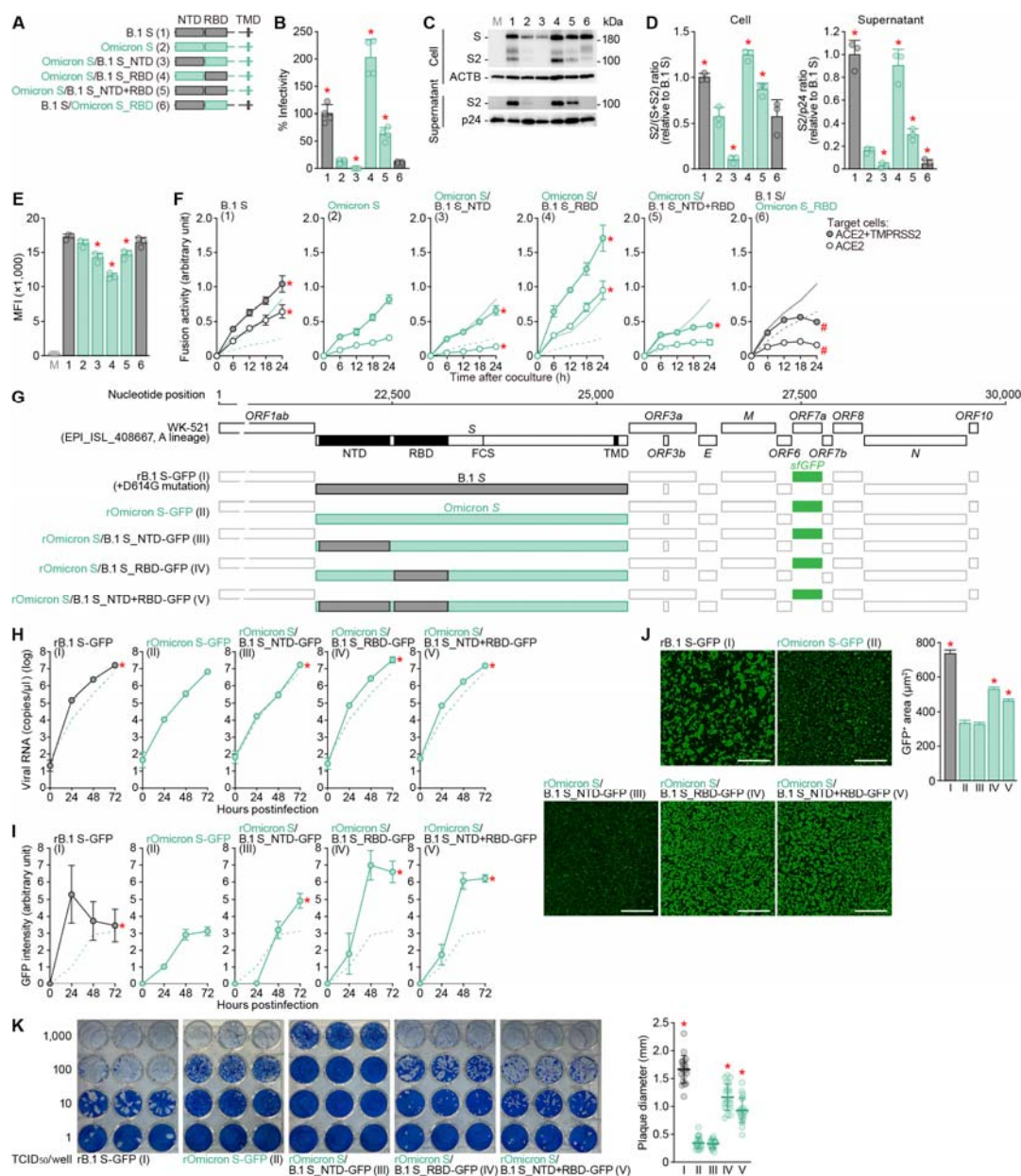


**Figure 1. Virological properties conferred by the Omicron RBD.**

(A) Scheme of S chimeras used in this study. The numbers in parentheses are identical to those in **Figures 1B-1E** and **2**. NTD, N-terminal domain; RBD, receptor-binding domain; TMD, transmembrane domain.

(B) Pseudovirus assay. HIV-1-based reporter viruses pseudotyped with SARS-CoV-2 S chimeras (summarized in **Figure 1A**) were prepared. The pseudoviruses were inoculated into HOS-ACE2/TMPRSS2 cells at 1,000 ng HIV-1 p24 antigen, and the percentages of infectivity compared to that of the virus pseudotyped with B.1 S (spike 1) are shown.

(C and D) Western blot. Representative blots of S-expressing cells and supernatants (C) and quantified band intensity (the ratio of S2 to the full-length S

plus S2 proteins for "cell"; the ratio of S2 to HIV-1 p24 for "supernatant") (**D**) are shown. M, mock (empty vector-transfected).

(**E**) Flow cytometry. The summarized results of the surface S expression are shown. MFI, mean fluorescent intensity; M, mock (empty vector-transfected).

(**F**) SARS-CoV-2 S-based fusion assay. The fusion activity was measured as described in the STAR<sup>®</sup> METHODS, and fusion activity (arbitrary units) is shown. For the target cells, HEK293 cells expressing ACE2 and TMPRSS2 (filled) and HEK293 cells expressing ACE2 (open) were used. The results for B.1 S or Omicron S are shown in other panels as black and green lines, respectively. The results in HEK293-ACE2/TMPRSS2 cells and HEK293-ACE2 cells are shown as normal or broken lines, respectively.

(**G**) Scheme of the S-chimeric recombinant SARS-CoV-2 used in this study. FCS, furin cleavage site. The backbone is SARS-CoV-2 strain WK-521 (GISAID ID: EPI\_ISL\_408667, A lineage) (Torii *et al.*, 2021). Note that the *ORF7a* gene is swapped with the *sfGFP* gene. The numbers in parentheses are identical to those in **Figures 1H-1K**.

(**H-J**) SARS-CoV-2 infection. VeroE6/TMPRSS2 cells were infected with a series of chimeric recombinant SARS-CoV-2 (shown in **G**) at multiplicity of infection (m.o.i.) 0.01. Viral RNA in the supernatant (**H**) and GFP intensity (**I**) were measured using routine techniques. The result for Omicron (virus II) is shown in other panels as a broken green line. (**J**) Syncytium formation. Left, GFP-positive area at 48 h.p.i. Scale bar, 500  $\mu$ m. Right, summarized results. I, n=6,483 cells; II, n=5,393 cells; III, n=8,704 cells; IV, n=13,188 cells; and V, n=12,749 cells. Representative images are shown in **Figure S1**.

(**K**) Plaque assay. Left, representative figures. Right, summary of the plaque diameters (20 plaques per virus).

Data are expressed as the mean with SD (**B**, **D-F**, **H** and **K**) or the median with 95% confidence interval (CI) (**J**).

Assays were performed in quadruplicate (**B**, **H**) or triplicate (**D-F**).

Each dot indicates the result of an individual replicate (**B**, **D** and **E**) or an individual plaque (**K**).

Statistically significant differences (\* $P < 0.05$ ) versus Omicron S (pseudovirus 2 for **B**, **D** and **E**, virus II for **J** and **K**) were determined by two-sided Student's t test (**B** and **E**), two-sided paired t test (**D**), or two-sided Mann–Whitney U test (**J** and **K**).

In **F**, **H** and **I**, statistically significant differences [\*familywise error rates (FWERs)  $< 0.05$ ] versus Omicron (spike 2 or virus II) (except for the rightmost panel in **F**) or B.1 (spike 1 or virus I) (rightmost panel in **F**) through timepoints were determined by multiple regression. FWERs were calculated using the Holm method.

See also **Figure S1**.

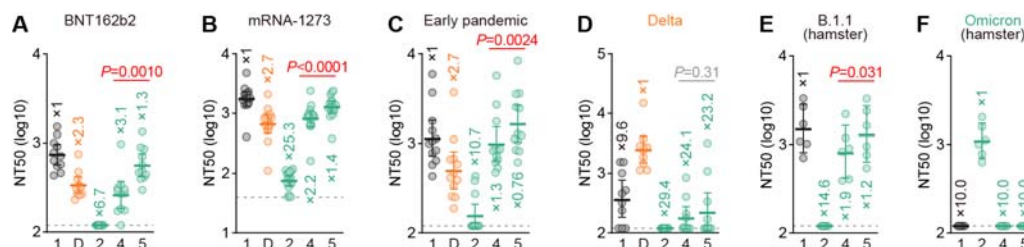


**Figure 2. Immune resistance conferred by the Omicron RBD.**

Neutralization assays were performed with pseudoviruses harboring a series of S protein sequences (summarized in **Figure 1A**). The numbers are identical to those in **Figure 1A**. D, Delta variant. Vaccinated sera [BNT162b2 (**A**, 11 donors); or mRNA-1273 (**B**, 16 donors)], convalescent sera of individuals infected with an early pandemic virus (before May 2020) (**C**, 12 donors), or Delta (**D**, 10 donors) and convalescent sera of hamsters infected with B.1.1 (**E**, 6 hamsters) or Omicron (**F**, 6 hamsters) were used. The list of sera used in this experiment is shown in **Table S1**. Each serum sample was analyzed in triplicate to determine the 50% neutralization titer (NT50). Each dot represents one NT50 value, and the geometric mean and 95% CI are shown. The numbers indicate the fold changes of resistance versus each antigenic variant. Horizontal gray lines indicate the detection limit of each assay (120 for **A** and **C-F**; 40 for **B**). Statistically significant differences between spikes 4 and 5 were determined by a two-sided Wilcoxon signed-rank test.

**See also Table S1.**



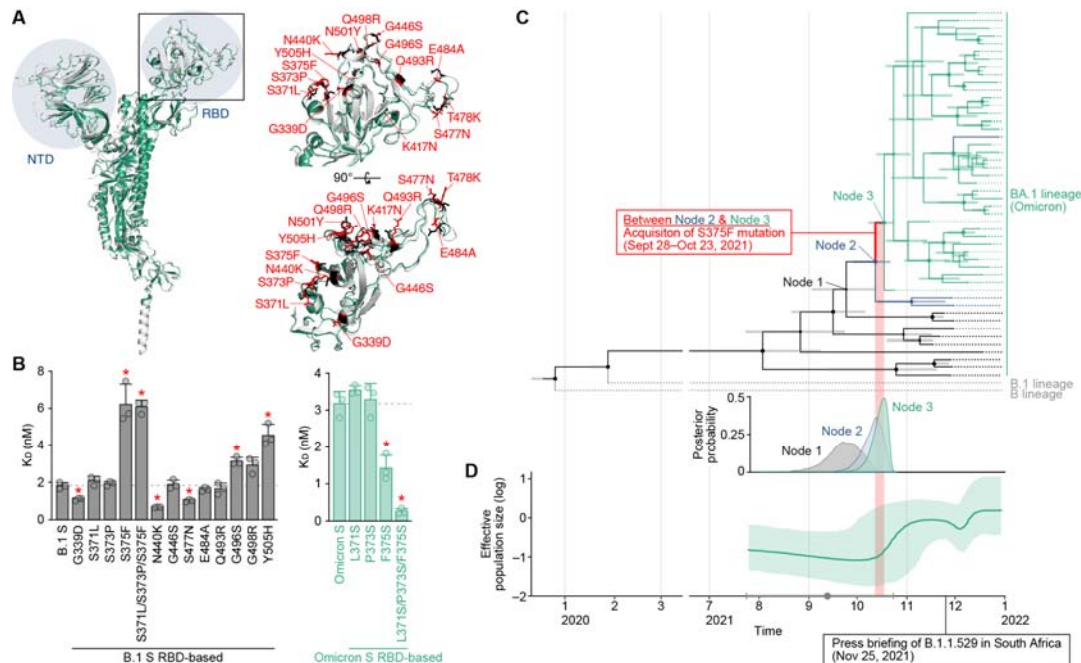


**Figure 3. Mutations in the Omicron RBD and the evolution of Omicron.**

**(A)** Structural insights into the mutations in the Omicron RBD. Left, overlaid crystal structures of SARS-CoV-2 B.1 S (PDB: 7KRQ) (Zhang et al., 2021) (white) and Omicron S (PDB: 7T9J) (Mannar et al., 2022) (green) are shown. The NTD and RBD are indicated in blue. The region in the RBD indicated by a square is enlarged in the top right panel. Right, mutated residues in the RBD. The residues in B.1 S and Omicron S are shown in black and red, and the mutations in Omicron S are indicated.

**(B)** ACE2 binding affinity of a series of SARS-CoV-2 S RBD (residues 336-528) mutants tested by yeast surface display. The  $K_D$  values of the binding of the SARS-CoV-2 S RBD expressed on yeast to soluble ACE2 are shown.

**(C and D)** Evolution of Omicron. **(C)** Top, a time tree of 48 Omicron variants and two outgroups (B and B.1 lineages). The same tree annotated with the GISAID ID, PANGO lineage and sampling date at each terminal node is shown in **Figure S2**. Green, Omicron variants containing the S371L, S373P and S375F mutations; blue, Omicron variants containing the S371L and S373P mutations; black, Omicron variants without the S371L/S373P/S375F mutations; and gray, the two outgroups (B and B.1 lineages). The bars on each internal node indicate the 95% highest posterior density (HPD) interval of the estimated time. Note that "Node 1" corresponds to the time to before the emergence of the S371L and S373P mutations; "Node 2" corresponds to the time after the acquisition of the S371L and S373P mutations and before the emergence of the S375F mutations; and "Node 3" corresponds to the fixation time of the S371L/S373P/S375F mutations in the Omicron variants. The estimated time of each node is as follows: Node 1, September 23, 2021 (95% HPD September 2, 2021 to October

1186 13, 2021); Node 2, October 11, 2021 (95% HPD September 28, 2021 to October  
1187 21, 2021); and Node 3, October 16, 2021 (95% HPD October 7, 2021 to October  
1188 23, 2021). Bottom, distribution of the posterior probability of the time to the  
1189 tMRCA of Node 1 (black), Node 2 (blue), and Node 3 (green). **(D)** Bayesian  
1190 skyline plot showing the history of the effective population size of 48 Omicron  
1191 variants. The 95% HPD is shaded in red. The dot (in gray) indicates the  
1192 estimated tMRCA of the 48 variants (September 12, 2021), and the error bar (in  
1193 gray) indicates the lower (July 24, 2021) and upper (October 23, 2021)  
1194 boundaries of the 95% HPD tMRCA.

1195 In **B**, the data are expressed as the mean with SD. The assay was performed in  
1196 triplicate, and each dot indicates the result of an individual replicate. The  
1197 horizontal broken lines indicate the value of B.1 S (left) and Omicron S (right),  
1198 respectively. Statistically significant differences (\* $P < 0.05$ ) versus B.1 S (left) or  
1199 Omicron S (right) were determined by two-sided Student's *t* tests, and FWERs  
1200 were calculated using the Holm method.

1201 In **C** and **D**, the timeline on the x-axis was shared, and the time of S375F  
1202 emergence (i.e., between “Node 2” and “Node 3” in **C**) is shaded in red.  
1203 See also **Figure S2**.



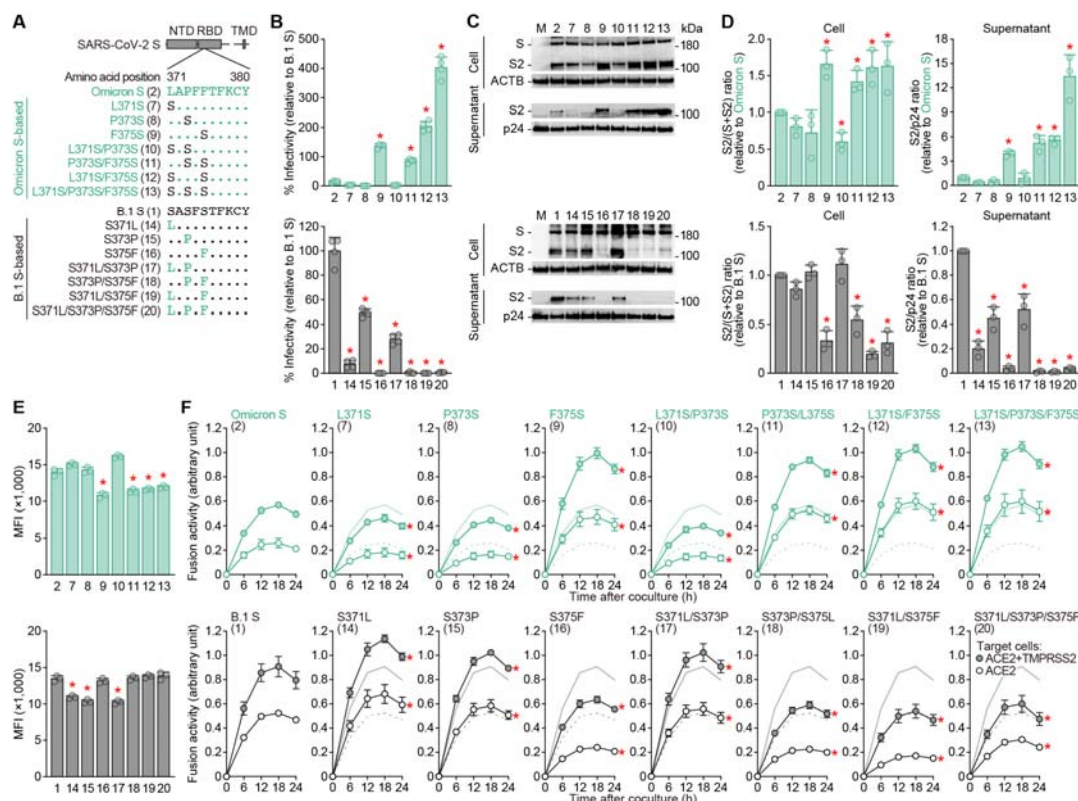


**Figure 4. Virological features conferred by the S S375F mutation.**

(A) Scheme of the S mutants used in this study. The numbers in parentheses are identical to those in Figures 4B-4F and S3.

(B) Pseudovirus assay. HIV-1-based reporter viruses pseudotyped with SARS-CoV-2 S mutants (summarized in A) were prepared. The pseudoviruses were inoculated into HOS-ACE2/TMPRSS2 cells at 1,000 ng HIV-1 p24 antigen, and the percent infectivity compared to that of the virus pseudotyped with Omicron S (spike 2, top) or B.1 S (spike 1, bottom) are shown.

(C and D) Western blot. Representative blots of S-expressing cells and supernatants (C) and quantified band intensity (the ratio of S2 to the full-length S plus S2 proteins for "cell"; the ratio of S2 to HIV-1 p24 for "supernatant") (D) are shown. M, mock (empty vector-transfected).

(E) Flow cytometry. The summarized results of the surface S expression are shown.

(F) SARS-CoV-2 S-based fusion assay. The fusion activity was measured as described in STAR METHODS, and fusion activity (arbitrary units) is shown. For the target cells, HEK293 cells expressing ACE2 and TMPRSS2 (filled) and HEK293 cells expressing ACE2 (open) were used. The results for Omicron S (top) or B.1 S (bottom) are shown in other panels as green and black lines, respectively. The results in HEK293-ACE2/TMPRSS2 cells and HEK293-ACE2 cells are shown as normal and broken lines, respectively.

Data are expressed as the mean with SD.

1227 Assays were performed in quadruplicate (**B**) or triplicate (**D-F**).  
 1228 In **B, D and E**, each dot indicates the result of an individual replicate.  
 1229 Statistically significant differences (\* $P < 0.05$ ) versus the respective parental S  
 1230 [Omicron S (pseudovirus 2, top panels) or B.1 S (spike 1, bottom panels)] were  
 1231 determined by two-sided Student's t test (**B and E**) or two-sided paired t test (**D**).  
 1232 In **F**, statistically significant differences (\*FWERs  $< 0.05$ ) versus the respective  
 1233 parental S [Omicron S (spike 2, top panels) or B.1 S (spike 1, bottom panels)]  
 1234 through timepoints were determined by multiple regression. FWERs were  
 1235 calculated using the Holm method.  
 1236 See also **Figure S3**.

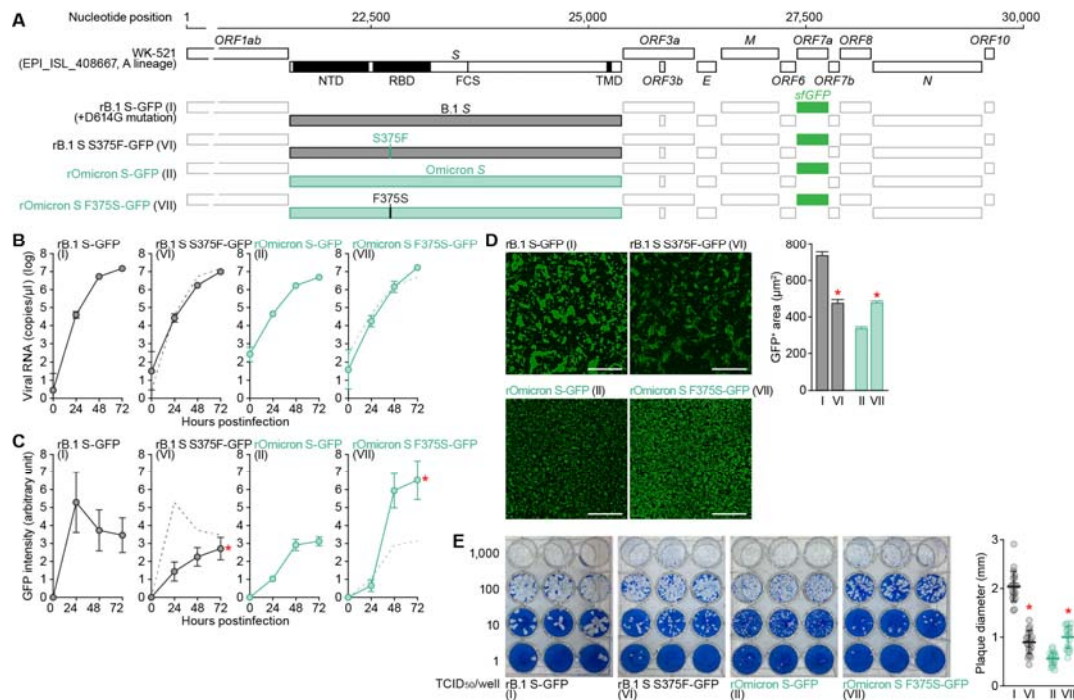


**Figure 5. Effect of the S S375F mutation on viral growth dynamics.**

**(A)** Scheme of the S-chimeric recombinant SARS-CoV-2 used in this study. The numbers in parentheses are identical to those in **Figures 5B-5E**.

**(B-D)** SARS-CoV-2 infection. VeroE6/TMPRSS2 cells were infected with a series of S-chimeric recombinant SARS-CoV-2 (summarized in **A**) at an m.o.i. 0.01. The viral RNA in the supernatant (**B**) and GFP intensity (**C**) were measured routinely. The results for the respective parental S are shown in other panels as broken green lines. Assays were performed in quadruplicate (**B and C**).

**(D)** Syncytium formation. Left, GFP-positive area at 48 h.p.i. Scale bar, 500 μm. Right, summarized results. I, n=6,483 cells; VI, n=2,780 cells; II, n=5,393 cells; and VII, 12,857 cells. The results for B.1-GFP (virus I) and Omicron-GFP (virus II) in **C** and **D** (right) are identical to those shown in **Figures 1I and 1J** (right). Representative images are shown in **Figure S1**.

**(E)** Plaque assay. Left, representative figures. Right, summary of the plaque diameters (20 plaques per virus). Each dot indicates the result of an individual plaque.

Data are expressed as the mean with SD (**B and E**) or the median with 95% CI (**D**).

In **B and C**, statistically significant differences (\*FWERs<0.05) versus Omicron-GFP (virus II) through timepoints were determined by multiple regression. FWERs were calculated using the Holm method.

In **D and E**, statistically significant differences (\*P<0.05) versus Omicron-GFP (virus II) were determined by a two-sided Mann–Whitney U test.

See also **Figure S1**.

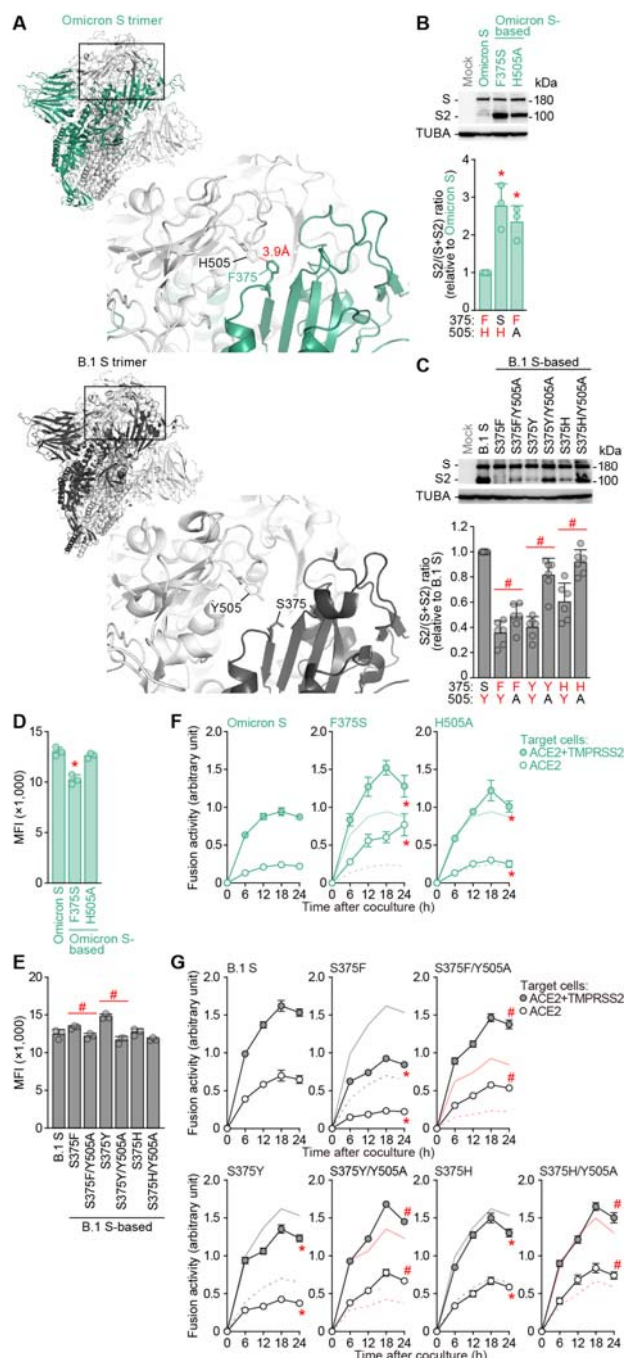


**Figure 6. Effect of the pi-pi interaction between 375F and 505H.**

**(A)** Structural insights into the SARS-CoV-2 S trimer. Top, the structure of the Omicron S trimer (PDB: 7T9J) (Mannar *et al.*, 2022) reconstructed as described in the STAR $\pi$ METHODS. Bottom, crystal structure of the B.1 S trimer (PDB: 7KRQ) (Zhang *et al.*, 2021). The regions indicated in squared are enlarged in the bottom right panels. In the enlarged panels, the residues at position 375 [F in an Omicron S monomer indicated in green (top); S in a B.1 S monomer indicated in black (bottom)] and 505 [H in an Omicron S monomer indicated in white (top); Y in a B.1 S monomer indicated in white (bottom)] are shown. The putative pi-pi

1272 interaction between F375 and H505 in the Omicron S trimer is indicated in red  
1273 (3.9 Å).  
1274 **(B and C)** Western blot. Representative blots of S-expressing cells (top) and  
1275 quantified band intensity (the ratio of S2 to the full-length S plus S2 proteins)  
1276 (bottom) are shown. In the bottom panels, the residues at positions 375 and 505  
1277 are indicated, and aromatic residues (F, H or Y) are indicated in red.  
1278 **(D and E)** Flow cytometry. The summarized results of the surface S expression  
1279 are shown.  
1280 **(F and G)** SARS-CoV-2 S-based fusion assay. The fusion activity was  
1281 measured as described in the STAR<sup>®</sup>METHODS, and fusion activity (arbitrary  
1282 units) is shown. For the target cells, HEK293 cells expressing ACE2 and  
1283 TMPRSS2 (filled) and HEK293 cells expressing ACE2 (open) were used. In **F**,  
1284 normal lines, Omicron S with HEK293-ACE2/TMPRSS2 cells; broken lines,  
1285 Omicron S with HEK293-ACE2 cells. In the panels of S375F, S375Y and S375H  
1286 in **G**, normal black lines, B.1 S using HEK293-ACE2/TMPRSS2 cells; broken  
1287 black lines, B.1 S using HEK293-ACE2 cells; normal red lines. In the panels for  
1288 S375F/Y505A, S375Y/Y505A and S375H/Y505A in **G**, normal red line, the result  
1289 for the respective mutant without the Y505A mutation using  
1290 HEK293-ACE2/TMPRSS2 cells; broken red line, the result for the respective  
1291 mutant without the Y505A mutation using HEK293-ACE2 cells.  
1292 Data are expressed as the mean with SD.  
1293 Assays were performed in triplicate (**B, D-G**) or sextuplicate (**C**).  
1294 In **B-E**, each dot indicates the result of an individual replicate.  
1295 Statistically significant differences versus Omicron S (\*P<0.05) and between the  
1296 mutant with and without the Y505A mutation (#P<0.05) were determined by  
1297 two-sided paired t test (**B and C**) or two-sided Student's t test (**D and E**).  
1298 In **F and G**, statistically significant differences versus Omicron S (\*FWERs<0.05)  
1299 or the mutant without the Y505A mutation (#FWERs<0.05) through timepoints  
1300 were determined by multiple regression. FWERs were calculated using the Holm  
1301 method.



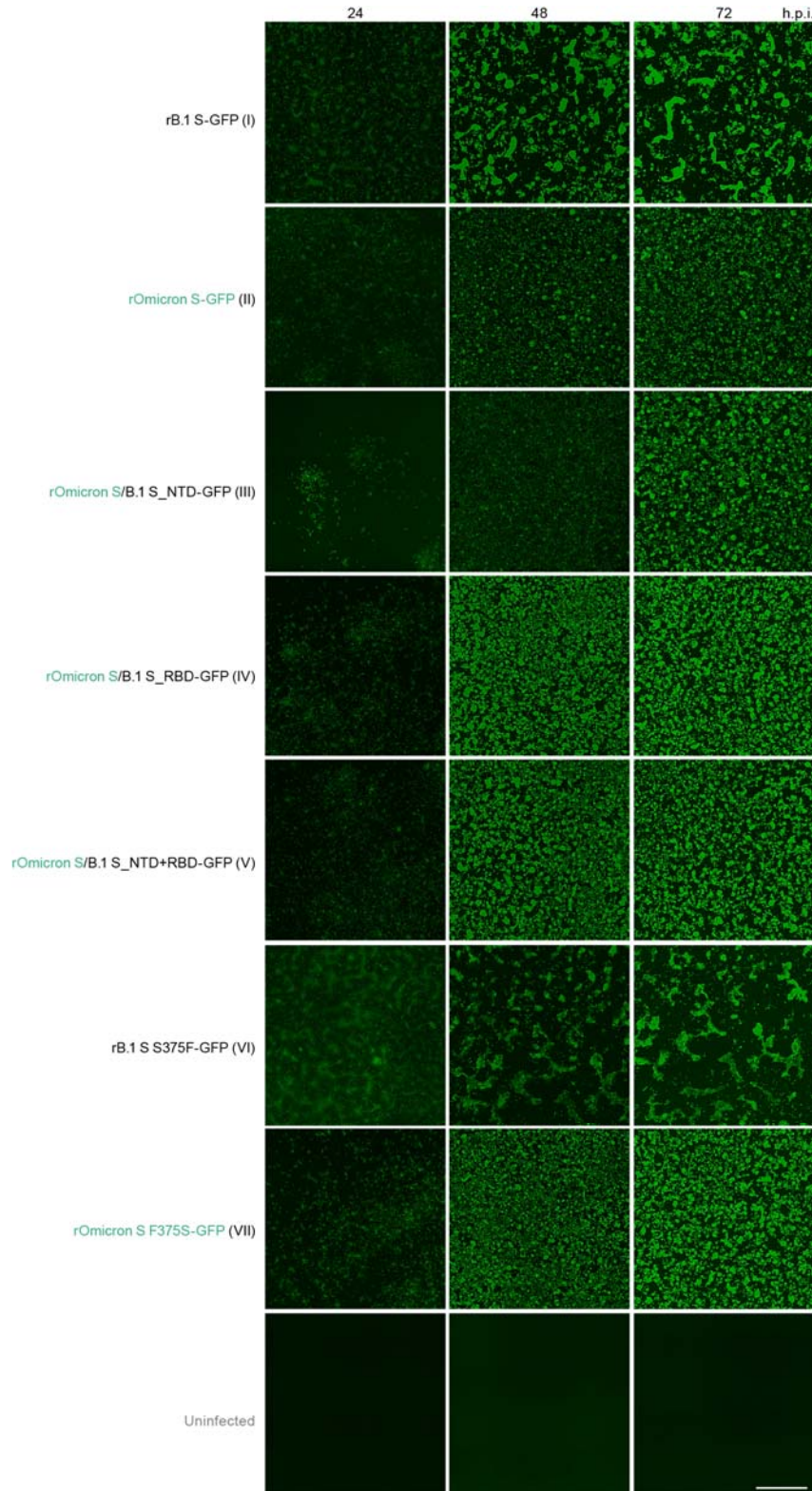


**Figure S1. Representative images of chimeric recombinant SARS-CoV-2-infected cells, related to Figures 1 and 5.**



1305 Fluorescence microscopy to measure the GFP area were measured in infected  
1306 VeroE6/TMPRSS2 cells (m.o.i. 0.01) at 24, 48, and 72 h.p.i. The panels at 48  
1307 h.p.i. are identical to those shown in **Figures 1J and 5D**. Scale bar, 500  $\mu$ m.

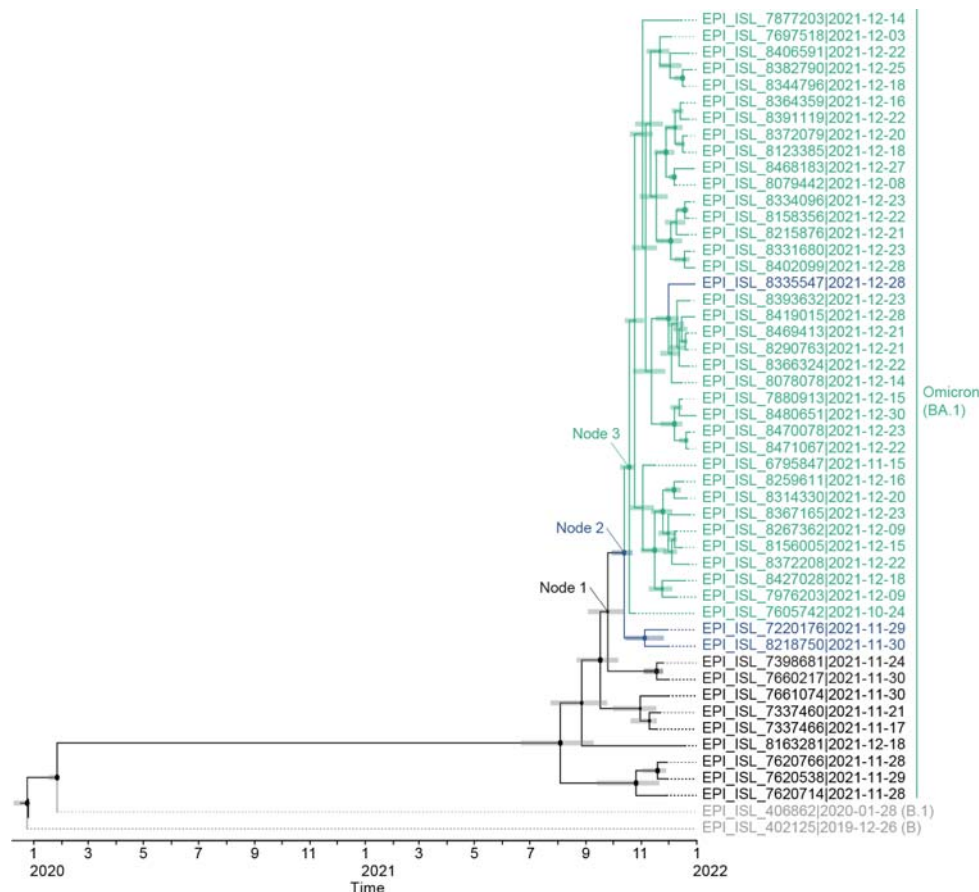


**Figure S2. Evolutionary of Omicron.**

A timetree of 48 Omicron variants and two outgroups (B and B.1 lineages) with GISAID ID, PANGO lineage and sampling date. The topology of the phylogenetic tree is identical to that shown in Figure 3C, top. Green, Omicron variants containing S371L, S373P and S375F mutations; blue, Omicron variants containing the S371L and S373P mutations; black, Omicron variants without the S371L/S373P/S375F mutations; and gray, the two outgroups (B and B.1 lineages). Bars on each internal node indicate the 95% HPD interval of estimation time.

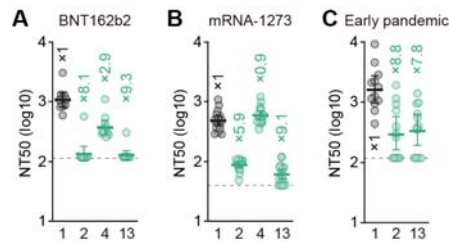


**Figure S3. Immune resistance of the Omicron S S371L/S373P/S375F mutant.**

Neutralization assays were performed with pseudoviruses harboring a series of S proteins (summarized in **Figures 1A and 4A**). The numbers are identical to those in **Figures 1A and 4A**. Vaccinated sera [BNT162b2 (**A**, 11 donors); or mRNA-1273 (**B**, 16 donors)] and convalescent sera of individuals infected with an early pandemic virus (until May 2020) (**C**, 12 donors) were used. The list of sera used in this experiment is shown in **Table S1**. Each serum sample was tested in triplicate to determine the 50% neutralization titer (NT50). Each dot represents one NT50 value, and the geometric mean and 95% CI are shown. The numbers indicate the fold changes of resistance versus each antigenic variant. Horizontal gray lines indicate the detection limit of each assay (120 for **A** and **C**; 40 for **B**).

1332	<b>Table S1. Human sera used in this study, related to Figure 2</b>
1333	
1334	<b>Table S2. Mutations detected in the Omicron RBD, related to Figure 3.</b>
1335	
1336	<b>Table S3. Primers used in this study, related to Figures 1 and 3–6.</b>
1337	
1338	<b>Table S4. Summary of the mutations detected in the working virus stocks</b>
1339	<b>compared to the original sequences, related to Figures 1 and 5</b>